Heterozygosity for neurodevelopmental disorder-associated *TRIO* variants yields distinct deficits in behavior, neuronal development, and synaptic transmission in mice.

Yevheniia Ishchenko*[1,2], Amanda T. Jeng*[1,3], Shufang Feng[1,4], Timothy Nottoli[5], Cindy Manriquez-Rodriguez[6], Khanh K. Nguyen[6], Melissa G. Carrizales[1,2], Matthew J. Vitarelli[1,2], Ellen E. Corcoran[1,2], Charles A. Greer[3,2,7], Samuel A. Myers[6], Anthony J. Koleske[1,2,3]

1. Department of Molecular Biophysics and Biochemistry, Yale University, New Haven, CT, USA
2. Department of Neuroscience, Yale School of Medicine, New Haven, CT, USA
3. Interdepartmental Neuroscience Program, Yale University, New Haven, CT, USA
4. Department of Gerontology, The Third Medical Center, Chinese PLA General Hospital, Beijing, China
5. Department of Comparative Medicine, Yale School of Medicine, New Haven, CT, USA
6. Laboratory for Immunochemical Circuits, La Jolla Institute for Immunology, La Jolla, CA, USA
7. Department of Neurosurgery, Yale School of Medicine, New Haven, CT, USA

* These authors contributed equally to this work.

ABSTRACT

Genetic variants in *TRIO* are associated with neurodevelopmental disorders (NDDs) including schizophrenia (SCZ), autism spectrum disorder (ASD) and intellectual disability. TRIO uses its two guanine nucleotide exchange factor (GEF) domains to activate GTPases (GEF1: Rac1 and RhoG; GEF2: RhoA) that control neuronal development and connectivity. It remains unclear how discrete *TRIO* variants differentially impact these neurodevelopmental events. Here, we investigate how heterozygosity for NDD-associated *Trio* variants – *+/K1431M* (ASD), *+/K1918X* (SCZ), and *+/M2145T* (bipolar disorder, BPD) – impact mouse behavior, brain development, and synapse structure and function. Heterozygosity for different *Trio* variants impacts motor, social, and cognitive behaviors in distinct ways that model clinical phenotypes in humans. *Trio* variants differentially impact head and brain size, with corresponding changes in dendritic arbors of motor cortex layer 5 pyramidal neurons (M1 L5 PNs). Although neuronal structure was only modestly altered in the *Trio* variant heterozygotes, we observe significant changes in synaptic function and plasticity. We also identified distinct changes in glutamate synaptic release in *+/K1431M* and *+/M2145T* cortico-cortical synapses. The TRIO K1431M GEF1 domain has impaired ability to promote GTP exchange on Rac1, but *+/K1431M* mice exhibit increased Rac1 activity, associated with increased levels of the Rac1 GEF Tiam1. Acute Rac1 inhibition with NSC23766 rescued glutamate release deficits in *+/K1431M* variant cortex. Our work reveals that discrete NDD-associated *Trio* variants yield overlapping but distinct phenotypes in mice, demonstrates an essential role for Trio in presynaptic glutamate release, and underscores the importance of studying the impact of variant heterozygosity in vivo.

INTRODUCTION

Neurodevelopmental disorders (NDDs), including autism spectrum disorder (ASD), intellectual disability (ID), developmental delay (DD), schizophrenia (SCZ) and bipolar disorder (BPD), disrupt brain development and function. NDDs share considerable comorbidities and present with overlapping symptoms, including impairments in cognition, behavior, language, social and motor skills, emotions, and learning ability (1). In addition, NDDs share many risk genes, further suggesting shared mechanistic underpinnings and pathology for these disorders (2). A major challenge remains in understanding how diverse risk-conferring variants contribute to the pathophysiology of various NDDs.

TRIO encodes a large cytoskeletal regulatory protein with two guanine nucleotide exchange factor (GEF) domains for Rho family GTPases - GEF1 activates Rac1 and RhoG, while GEF2 activates RhoA (3-5). TRIO relays signals from cell surface receptors, acting on GTPases to coordinate cytoskeletal rearrangements critical for proper neurodevelopment (6-14). *Trio* knockout mice exhibit decreased survival, skeletal muscle defects, and severe defects in brain development (15-17). Selective ablation of *Trio* in either excitatory or inhibitory neurons alters their morphology, impairs synaptic signaling, and yields NDD-related behavioral defects (18, 19). Trio deficiency also leads to aberrations in long-term potentiation (LTP), as Trio-Rac1 signaling promotes AMPA receptor trafficking to increase synaptic strength (18, 20, 21).

Damaging *de novo* mutations and ultra-rare variants in *TRIO* are enriched in individuals with NDDs (22-29). Interestingly, nonsense variants spread throughout *TRIO* are enriched in individuals with SCZ (29, 30), whereas pathogenic missense *TRIO* variants in or surrounding the GEF1 domain are associated with ASD/ID (23, 27, 28). Variants in the TRIO GEF1 domain that decrease Rac1 activity are associated with milder ID and microcephaly, whereas variants in the adjacent spectrin repeat 8 domain that increase Rac1 activity are associated with more severe ID and macrocephaly (24, 25, 31, 32). Rare missense variants in *TRIO* have also been observed in BPD, epilepsy, and other disorders, but studies to date are underpowered to establish a causal link with these disorders. Given the wide spectrum of *TRIO* variants associated with different pathological conditions, a fundamental and unresolved question is the mechanisms by which distinct *TRIO* variants differentially impact normal mammalian brain development and function. NDD-associated *TRIO* variants affect in vitro GEF1 and GEF2 activities, cell morphology, inhibitory neuron maturation, axon guidance, and synapse function (18-20, 32-34); however, the impact of heterozygosity for distinct *TRIO* variants in vivo, as found in individuals with NDDs, has been unexplored.

We report here the comprehensive analysis of mice heterozygous for discrete *Trio* variants impacting Trio functional domains and associated with different NDDs: *+/K1431M* in the Trio GEF1 domain associated with ASD, *+/K1918X* leading to nonsense decay associated with SCZ, and *+/M2145T* in the Trio GEF2 domain, a de novo mutation found in an individual with BPD that impacts GEF2 activity. We show that these distinct *Trio* NDD-associated variants differentially impair mouse behavior, brain development, and inhibitory and excitatory synaptic transmission. We show, for the first time, that *Trio* variants that impact GEF1 and GEF2 activity differentially impact presynaptic neurotransmitter release and synaptic vesicle replenishment. In addition, we found that while the K1431M mutation impairs Trio GEF1 activation of Rac1 in vitro, *+/K1431M* mice exhibit increased levels of active Rac1. This was associated with increased levels of the Rac1 GEF Tiam1, and acute Rac1 inhibition with NSC23766 rescued glutamate release deficits in *+/K1431M* variant cortex. Together, our data show how discrete heterozygous *TRIO* variants that differentially impact Trio biochemical activities yield divergent effects on behavior, neurodevelopment, and synaptic transmission.

MATERIALS AND METHODS

Key Resources Table

Reagent type (species) or resource	Designation	Source or reference	Identifiers	Additional information
Strain, strain background (*Mus musculus*)	*Trio*$^{+/K1431M}$ *Trio*$^{+/K1918X}$ *Trio*$^{+/M2145T}$ *Trio*$^{+/+}$(C57Bl/6)	This paper Jax Laboratories (by Dr. CC Little)	 RRID:IMSR JAX:000664	Both sexes
Sequence-based reagent	5'-tgtaatacgactcactatagg ACCTGATCAAACCA GTTCAGgttttagagctag aaatagc-3'	This paper	sgRNA scaffold sequence *K1431M*	
Sequence-based reagent	5'-tgtaatacgactcactatagg AAGCTTCTCACGCA CGCAGGgttttagagctag aaatagc-3'	This paper	sgRNA scaffold sequence *K1918X*	
Sequence-based reagent	5'-tgtaatacgactcactatagg ATGACATGATGAAC GTCGGGgttttagagctag aaatagc-3'	This paper	sgRNA scaffold sequence *M2145T*	
Sequence-based reagent	5'-gccaattccatctcttcctACC TGATCAAACC***T***GT***A***C AGCG***T***ataacaa***T***gtatc agctccttttaaaggtgtgtatg aaacattgtccatctgcaacat cacaccctgtgttgatatgtatc ccct-3'	This paper	Recombination template oligos *K1431M*	silent mutations bolded and italicized; new restriction digest site underlined (creates BsrGI site)
Sequence-based reagent	5'-agctgccatctatggcaaagg catttgtacacaggtgtgaga gtgactcgcgaa***A***CT***G***CT GC***A***TGCGTGAGAAG CTTaccattttgcttt***A***cacg agttcttcaatagcactgacga gctcagctgcgctgggag-3'	This paper	Recombination template oligos for *K1918X*	silent mutations bolded and italicized; new restriction digest site underlined (creates SphI site)
Sequence-based reagent	5'-agggcccctcaataaacaat gcattacgtcaaatccctgca G***T***CG***A***C***A***acgttcatc ***G***tgtcattacagcgcttcggc acgatgcacatgacttctaca gctttctgtgggtggagagaa agca-3'	This paper	Recombination template oligos for *M2145T*	silent mutations bolded and italicized; new restriction digest site underlined (creates SalI site)
Sequence-based reagent	*primer pairs: GFP_For: 5'-gcacgacttcttcaagtccgc*	This paper		Mice genotyping

	catgcc-3' *GFP_Rev: 5'-gcggatcttgaagttcaccttgatgcc-3'*			
Sequence-based reagent	*primer pairs:* *Trio1431_For: 5'-ttgtcattaatgtggtactgtgcc-3'* *Trio1431_Rev: 5'-gacaggccaagaaatgtcagtg-3'*	This paper		Mice genotyping
Sequence-based reagent	*primer pairs:* *Trio1918_For: 5'-tacgagggagttcactgtctg-3'* *Trio1918_Rev: 5'-agtgcaggctatgcttcgttta-3'*	This paper		Mice genotyping
Sequence-based reagent	*primer pairs:* *Trio2145_For: 5'-gcctggacacatccgaattaga-3'* *Trio2145_Rev: 5'-aataaccccggacagaggaaag-3'*	This paper		Mice genotyping
Antibody	Rabbit anti-TRIO SR5-6	Katrancha et al 2019		WB (1:1000)
Antibody	Rabbit anti-TRIO DH2	Katrancha et al 2019		WB (1:1000)
Antibody	Mouse anti-PSD95	NeuroMab	Cat#: K28/43	WB (1:5000)
Antibody	Rabbit anti-Synaptophysin (Syp)	Cell Signaling	Cat#: 36406S	WB (1:5000)
Antibody	Rabbit anti-Munc18-1/Stxbp-1	Abcam	Cat#: 109023	WB (1:1000)
Antibody	Rabbit anti-Syntaxin-1a (Stx1a)	Synaptic Systems	Cat#: 110 118	WB (1:5000)
Antibody	Rabbit anti-Synaptotagmin3 (Syt3)	Synaptic Systems	Cat#: 105 133	WB (1:500)
Antibody	Rabbit anti-Kalirin (CT302)	Yan et al 2015		WB (1:1000)
Antibody	Rabbit anti-Tiam1	Cell Signaling	Cat#: 31128	WB (1:1000)
Antibody	Rabbit anti-VAV2	Abcam	Cat#: 52640	WB (1:5000)
Antibody	Goat anti-Rabbit IgG(H+L)-HRP conjugate	Bio-Rad	Cat#: 170-6515	WB (1:5000)
Antibody	Goat anti-Mouse IgG(H+L)-HRP conjugate	Bio-Rad	Cat#: 172-1011	WB (1:5000)
Antibody	Chicken anti-NeuN	Synaptic Systems	Cat#: 266 006	IF (1:2000)

Antibody	Guinea pig anti-Parvalbumin (PV)	Swant	Cat#: GP72	IF (1:1000)
Antibody	Goat anti-Chicken IgY(H+L), AlexaFluor 488	ThermoFisher	Cat#: A-11039	IF (1:2000)
Antibody	Goat anti-Rabbit IgG(H+L), AlexaFluor 568	ThermoFisher	Cat#: A-11011	IF (1:2000)
Commercial assay, kit	DAPI	Invitrogen	Cat#: D21490	IF (1:10,000)
Chemical compound, drug	Kynurenic acid	Tocris Bioscience	Cat# 3694	
Chemical compound, drug	Lidocaine N-ethyl bromide (QX-314)	Tocris Bioscience	Cat# 2313	
Chemical compound, drug	D-2-Amino-5-phosphonovaleric acid (D-AP5)	Tocris Bioscience	Cat# 0106	
Chemical compound, drug	(-)-bicuculline methochloride (BMI)	Tocris Bioscience	Cat# 0109	
Chemical compound, drug	Strychnine hydrochloride	Tocris Bioscience	Cat# 2785	
Chemical compound, drug	Cyanquixaline (CNQX)	Tocris Bioscience	Cat# 0190	
Chemical compound, drug	NSC23766	Tocris Bioscience	Cat# 2785	
Chemical compound, drug	Tetrodotoxin	Tocris Bioscience	Cat# 1078	
Recombinant DNA reagent (human)	WT TRIO GEF1	Blaise AM et.al. 2022		Used for recombinant protein purification
Recombinant DNA reagent (human)	*K1431M* TRIO GEF1	This paper		Used for recombinant protein purification
Recombinant DNA reagent (human)	Rac1	Blaise AM et.al. 2022		Used for recombinant protein purification
Sequence-based reagent	5'-cagcgaataacgatgtatcagctcc-3' and 5'-ggagctgatacatcgttattcgctg-3'.	This paper		Oligonucleotides for site-directed mutagenesis (K1431M TRIO GEF1)
Commercial assay, kit	BODIPY-FL-GDP	Invitrogene	Cat# G22360	
Commercial assay, kit	G-LISA activation assay kits for Rac1	Cytoskeleton Inc.	Cat# BK128	

Commercial assay, kit	G-LISA activation assay kits for RhoA	Cytoskeleton Inc.	Cat# BK124	
Software, algorithm	AnyMaze software	Stoelting Co.		Behavioral analysis
Software, algorithm	Fiji	https://fiji.sc/	RRID:SCR_002285	IF and WB analysis
Software, algorithm	Mini-Analysis software	Synaptosoft		mEPSCs analysis
Software, algorithm	Origin Version 2021	OriginLab	RRID: 2JJ-JT7-8IP	Electrophysiology graphing, signal processing, and analysis
Software, algorithm	GraphPad Prism	Dotmatics	V10	Statistical analysis and graphing
Software, algorithm	QuPath software	https://qupath.github.io/		Neuroanatomy analysis
Software, algorithm	pClamp software suite	Molecular Devices	11.1	Electrophysiolog recordings, y graphing, signal processing, and analysis

Animal work

All animal work was performed in compliance with federal guidelines and approved by the Yale Institutional Animal Care and Use Committee. All mice were maintained on a C57Bl/6 background and housed on a standard 12-hour light/dark cycle. Mice heterozygous for *Trio* variants *K1431M* (*Trio*$^{+/K1431M}$), *K1918X* (*Trio*$^{+/K1918X}$), or *M2145T* (*Trio*$^{+/M2145T}$) were crossed with WT (*Trio*$^{+/+}$) mice to produce heterozygous *Trio* variant and WT littermates used in all experiments. As the mice were maintained on the same genetic background, analyses of WT mice were pooled and considered one genotype, irrespective of parental *Trio* variant genotype. Age-matched mice of both sexes were used for behavioral experiments and for brain and body weight measurements. Only male mice were used for electrophysiological and neuroanatomical analyses to reduce potential variation in dendritic spines and activity due to estrus cycle (35).

Generation of *Trio* mutant mice

Mice heterozygous for *Trio* variants *K1431M*, *K1918X*, or *M2145T* were generated via CRISPR/Cas-mediated genome editing (36, 37). Potential Cas9 target guide (protospacer) sequences in the vicinity of the *Trio K1431*, *K1918*, and *M2145* codons were screened using the online tool CRISPOR (38) and candidates were selected. Templates for sgRNA synthesis were generated by PCR from a pX330 template (Addgene), sgRNAs were transcribed *in vitro* and purified (Megashortscript, MegaClear; ThermoFisher). sgRNA/Cas9 RNPs were complexed and tested for activity by zygote electroporation, incubation of

embryos to blastocyst stage, and genotype scoring of indel creation at the target sites. sgRNAs that demonstrated the highest activity were selected for creating the knock-in alleles. Guide primers for generating the template for transcription included a 5' T7 promoter and a 3' sgRNA scaffold sequence and were as follows (protospacer sequence capitalized):

K1431M: 5'-tgtaatacgactcactataggACCTGATCAAACCAGTTCAGgttttagagctagaaatagc-3'

K1918X: 5'-tgtaatacgactcactataggAAGCTTCTCACGCACGCAGGgttttagagctagaaatagc-3'

M2145T: 5'-tgtaatacgactcactataggATGACATGATGAACGTCGGGgttttagagctagaaatagc-3'

Recombination template oligos (Integrated DNA Technologies, San Diego CA) were designed to create the desired codon changes, with incorporation of silent mutations to destroy the PAM and prevent sgRNA recognition of the newly created alleles as well as create a new restriction site for genotyping. sgRNA/Cas9 RNP and the template oligo were electroporated into C57Bl/6J (JAX) zygotes (37). Embryos were transferred to the oviducts of pseudopregnant CD-1 foster females using standard techniques (39). Genotype screening of tissue biopsies from founder pups was performed by PCR amplification and Sanger sequencing to identify the desired base changes, followed by backcrossing to C57Bl/6 mice and sequence confirmation to establish germline transmission of the correctly targeted alleles. Recombination template oligos were as follows (silent mutations bolded and italicized; new restriction digest site underlined):

K1431M: 5'-
gccaattccatctcttcctACCTGATCAAACC***T***GT***A***CAGCG***T***ataacaa***T***gtatcagctccttttaaaggtgtgtat
gaaacattgtccatctgcaacatcacaccctgtgttgatatgtatcccct-3' (creates BsrGI site)

K1918X: 5'-
agctgccatctatggcaaaggcatttgtacacaggtgtgagagtgactcgcgaa***A***CT***G***CTGC***A***TGCGTGAGAA
GCTTaccattttgcttt***A***cacgagttcttcaatagcactgacgagctcagctgcgctgggag-3' (creates SphI site)

M2145T: 5'-
agggcccctcaataaacaatgcattacgtcaaatccctgcaG***T***CG***A***CC***A***acgttcatc***G***tgtcattacagcgcttcggca
cgatgcacatgacttctacagctttctgtgggtggagagaaagca-3' (creates SalI site)

Mouse genotyping

Genotypes were determined by PCR of mouse DNA using the following primer pairs:

GFP_For: 5'-gcacgacttcttcaagtccgccatgcc-3'

GFP_Rev: 5'-gcggatcttgaagttcaccttgatgcc-3'

Trio1431_For: 5'-ttgtcattaatgtggtactgtgccc-3'

Trio1431_Rev: 5'-gacaggccaagaaatgtcagtg-3'

Trio1918_For: 5'-tacgagggagttcactgtctg-3'

Trio1918_Rev: 5'-agtgcaggctatgcttcgttta-3'

Trio2145_For: 5'-gcctggacacatccgaattaga-3'

Trio2145_Rev: 5'-aataaccccggacagaggaaag-3'

To distinguish *Trio* variant and WT alleles, PCR was followed by restriction digest at 37°C for at least 4 hours (BsrGI for *K1431M*, SphI for *K1918X*, SalI for *M2145T*) and subjected to agarose gel electrophoresis.

WT samples resulted in a band at 530 kb for *K1431* litters, 550 kb for *K1918* litters, 400 kb for *M2145* litters; while *Trio* heterozygous variants resulted in bands at 450 and 530 kb for +/*K1431M*, 350 and 550 kb for +/*K1918X*, 350 and 400 kb for +/*M2145T*. All mice used in experiments were genotyped twice from DNA samples collected at two different time points, prior to weaning and again post-experiment for validation.

In vitro GEF Assays

The *K1431M* point mutant was generated via site-directed mutagenesis of human WT TRIO GEF1 using the following oligos: 5'-cagcgaataacgatgtatcagctcc-3' and 5'-ggagctgatacatcgttattcgctg-3'. Recombinant WT and *K1431M* human TRIO GEF1 and Rac1 proteins were purified from bacteria as previously described (40). GEF activity was monitored by the decrease in fluorescent signal ($\lambda_{excitation}$ = 488 nm; $\lambda_{emission}$ = 535 nm) as GTP was exchanged for BODIPY-FL-GDP on Rac1 over 30 min, as previously described (32, 40).

Body weight, brain weight, and head width measurements

Ear-to-ear head width of P42 mice was measured with calipers in anesthetized mice. Brain weight was measured after removing the olfactory bulbs and brain stem.

Brain lysate preparation

Whole brain lysates from P0-P1 or P35-P42 mice were prepared as previously described (18, 41, 42), with minor modifications. Cerebella, hippocampi, and cortices were rapidly removed, snap-frozen in liquid nitrogen and stored at -80°C until lysate preparation. Tissue was homogenized in ice-cold RIPA buffer (1% NP-40, 0.1% SDS, 50 mM Tris pH 8, 150 mM NaCl, 0.5% sodium deoxycholate) supplemented with protease and phosphatase inhibitors (Roche 11873580001; Roche 04906837001), then clarified by brief centrifugation; aliquots were snap frozen and stored at -80° C until immunoblotting. For Trio immunoblots, tissue was sonicated in homogenization buffer (1% SDS, 50 mM Tris pH 7.4, 2 mM EDTA), supplemented with protease and phosphatase inhibitors, heated at 95° C for 5 min, then

clarified, snap frozen, and stored at -80° C until immunoblotting. Protein concentrations were determined with a bicinchoninic acid (BCA) assay (Pierce).

Cortical synaptosome prep

Crude synaptosomes were prepared as previously described (41, 42). Briefly, cortices were rapidly dissected from anesthetized P39-P42 mice and immediately homogenized in cold buffer (118 mM NaCl, 4.7 mM KCl, 1.2 mM $MgSO_4$, 2.5 mM $CaCl_2$, 1.53 mM KH_2PO_4, 212.7 mM glucose) supplemented with protease and phosphatase inhibitors (Roche). Homogenates were passed through a series of nylon filters of descending pore size: 40 µm, 10 µm, and finally 5 µm. Samples were centrifuged for 15 min at 1,000 x g at 4°C; the supernatant was discarded, and the pellet was resuspended in an appropriate buffer for G-LISA measurements or immunoblotting. Mice from at least 3 litters per genotype were processed concurrently with WT littermates.

Western blot and quantification

Brain lysates were separated on SDS-PAGE gels, transferred to nitrocellulose membranes, stained with Ponceau S, blocked in 5% nonfat milk in TBS-T, and incubated with primary antibodies overnight at 4°C, then with conjugated secondary antibodies at RT for 1 h (see **Key Resources Table** for list of antibodies). Images were captured by a ChemiDoc Imaging System (Bio-Rad) and quantified in ImageJ. Signal intensity was normalized to Ponceau S, then to the WT average.

G-LISA

Active GTP-bound GTPase levels in brain lysates were measured using G-LISA activation assay kits for Rac1 (Cytoskeleton, Inc., BK128) and RhoA (Cytoskeleton, Inc., BK124). Brains or crude synaptosome pellets were homogenized in G-LISA lysis buffer supplemented with protease and phosphatase inhibitors (Roche), normalized to the same concentration as determined by Precision Red Advanced Protein Assay, and applied to the G-LISA matrices and processed according to manufacturer's protocols. Absorbances at 490 nm (OD_{490}) were background-subtracted and normalized to the WT average.

Behavioral tests

Behavioral tests were performed in both male and female mice 6-8 weeks of age (P42-P56). Mice were habituated to handling for 5 minutes per day for 5 days prior to experiments, and habituated in the test facility separate from housing for at least 30 minutes prior to starting the task. We performed the Kondziela inverted screen test for motor strength, accelerating rotarod for motor coordination and learning, social preference test, novel object recognition

task, open field test, elevated plus maze, and nestlet shredding, as previously described (18, 43-46). All behavioral studies were performed and analyzed by an experimenter blinded to genotype. Individual data points could be excluded from analysis if a mouse failed to properly acclimate to the testing conditions, as described in detail for specific tests below.

Accelerating rotarod

A five-lane rotarod treadmill (Med Associates ENV-577M 8.75'' rod circumference) was used for accelerating analyses. Mice were acclimated to the rotating rod at 4 RPM for 10 sec before beginning the test; mice that were unable to stay on the rod during this period were excluded from analyses. The rod then accelerated from 4 to 40 RPM over the course of 5 minutes (1.2 RPM/10 s) before leveling off at 40 RPM for 2.5 minutes. Five trials were performed per mouse with a rest time of at least 10 minutes between trials. The latency to fall was recorded per trial.

Kondziela inverted screen test

The screen apparatus consisted of a 40 cm square of wire mesh composed of 12 mm squares with 1 mm diameter wire, surrounded by a square wooden frame 3.5 cm thick. Mice were placed in the center of the screen and inverted over 2 seconds over a clear open box 45 cm high. During the training session on day 1, mice were habituated to hanging on the screen until a cumulative hang time of 2 minutes was reached; mice were excluded if they were unable to meet this requirement. During the test session on day 2, mice were placed on the screen as before and given 3 trials to reach a maximum inverted hang time of 8 minutes, with 10-minute rest periods between trials. Mice that were unsuccessful at reaching the 8-minute mark were excluded from the accelerating rotarod test.

Open field test

Mice were placed in a large 16x16 inch square clear plexiglass SuperFlex cage and monitored using the Fusion software connected to a light beam array (Omnitech Electronics, Open Field Test, Version 4.5) for 10 minutes. The following measurements were analyzed based upon beam breaks: total distance traveled, ambulatory time (successive beam breaks), and vertical activity time (z axis beam breaks).

Social preference test

Mice were placed in a 50 cm x 50 cm plexiglass box with two wire-mesh pencil holders (open side facing downward) for 10 minutes for habituation. Then, the mouse was briefly removed while an inanimate object (Duplo blocks of a similar size and color to a mouse) and a male conspecific ''stranger'' mouse were placed underneath separate wire-mesh pencil

holders. The test mouse was then returned to the cage for 10 minutes, tracked using the AnyMaze software (Stoelting Co.), and scored for entries into and time within a social target zone and an equivalent nonsocial target zone. The target zones were defined by an annulus around the wire enclosure.

Novel object recognition task

During object familiarization on day 1, two identical objects were placed on the left and right sides of the testing cage. Mice explored the objects until they accumulated 30 s of tactile exploration time, defined as direct oral or nasal contact. Mice were then returned to their home cage for 48 hours. During the novel object recognition task on day 3, one familiar and one novel object were placed on either side of the testing cage, and mice explored the objects until they accumulated 30 s of tactile exploration time. Mice were excluded from analysis if they failed to explore both objects or accumulate 30 s of tactile exploration time within 6 minutes on either day.

Elevated plus maze

The apparatus is raised 36.5 cm above the ground with a 5 cm square center platform and four 30 cm x 5 cm arms; two of the arms are enclosed by 16 cm high walls (Stoelting Co, Wood Dale, IL). Mice were tested in 3 trials that were 5 minutes long with at least 10 minutes to rest between trials. Mice were placed directly on the center platform and allowed to freely explore all arms of the maze, tracked using the AnyMaze software (Stoelting Co.), and scored for time spent in each arm.

Nestlet shredding

A standard polycarbonate mouse cage (19×29×13 cm) was filled with unscented bedding material to a depth of 0.5 cm, the surface was leveled, and a fitted filter-top cover was placed on top. Commercially available cotton fiber nestlets (5 cm x 5 cm, 5 mm thick, 2-2.5 g each) were weighed on an analytical balance before being placed on top of the bedding. The mouse was placed into the test cage without food or water and left undisturbed for 30 minutes. The remaining intact nestlet was removed and allowed to dry overnight. The weight of the dried unshredded nestlet was divided by the starting weight to calculate percentage of nestlet shredded.

Animal perfusion and tissue processing

Mice were transcardially perfused with heparinized PBS followed by 4% paraformaldehyde (PFA) in phosphate buffered saline (PBS). Brains were postfixed in 4% PFA at 4°C for 24 h, then sliced coronally at 30 µm for Nissl stain and immunohistochemistry and at 200 µm for

dendritic arbor and spine analysis. Sections were processed as per application and coverslip-mounted with ProLong Diamond Antifade Mountant (P36961, ThermoFisher). For electron microscopy, mice were perfused with 4% PFA supplemented with 2% glutaraldehyde.

Nissl staining

Nissl staining on 30 µm brain slices was performed according to standard protocols (47). Brightfield images were acquired at 20X on a SlideView VS200 slide scanner (Olympus). Coronal sections containing the decussation of the anterior commissure were selected for analysis and quantified using QuPath software. Measurements from three consecutive slices were averaged per mouse.

Immunostaining

Desired sections were identified by comparison to a mouse brain atlas (48). Three 30-µm coronal sections from the motor cortex, spaced at 120-µm intervals and containing the rostral decussation of the corpus callosum were used for immunostaining. Mounted sections were boiled in Na-Citrate buffer (10 mM, pH 6.4) for 45 min, blocked for 1 h in 5% normal goat serum (NGS) in 0.3% PBS-T, incubated overnight at 4°C with primary antibodies **(Key Resources Table)**, then with appropriate AlexaFluor-conjugated secondary antibodies for 1 h at RT, and counterstained for 10 min with DAPI. Controls lacking primary antibody were used to confirm staining specificity. Fluorescent images were acquired at 10X on a SlideView VS200 slide scanner (Olympus). Semi-automatic cell counts for DAPI+, NeuN+, and PV+ stained cells were obtained using QuPath by an experimenter blinded to genotype.

Dendritic arbor reconstructions and dendritic spine density analysis

Mice of all genotypes examined were intercrossed with mice bearing a *thy1-GFP* transgene (M line) (49). Fluorescent images of neurons contained within 200 µm coronal sections were acquired at 20X for arbor reconstructions (Zeiss LSM900) and at 100x on an UltraVIEW VoX spinning disc confocal microscope for dendritic spines. Dendrites were traced and measured using the Simple Neurite Tracer Fiji plugin (SNT) in ImageJ (NIH). Spines were manually counted from max projection z-stack images on secondary apical and basal dendritic branches of L5 PNs.

Electron microscopy

Electron microscopy of synapses in M1 layer 5 was performed as previously described (18). Asymmetric excitatory synapses were identified as an electron-dense post-synaptic density (PSD) apposed to a presynaptic terminal containing synaptic vesicles. Measurements of

synaptic features, including synapse density, PSD length, spine head area, presynaptic bouton area, and synaptic vesicle distribution, were quantified in ImageJ as previously described (50-53), from 5-18 fields of view (~50 μm^2) per mouse by a reviewer blinded to genotype.

Electrophysiological recordings

Acute slices were prepared from mice at P35-42 as previously described (18) with modifications noted here. Coronal slices of M1-M2 cortex were cut at 360 µm in ice-cold N-Methyl-D-glucamine-aCSF (NMDG-aCSF, in mM): 120 NMDG, 2.5 KCl, 7 $MgSO_4$, 1.25 NaH_2PO_4, 0.5 $CaCl_2$, 28 $NaHCO_3$, 13 glucose, 7 sucrose, saturated with 95% O2-5% O2 at 300-320 mOsmol/L, pH 7.4) on a vibratome (Leica). Slices were recovered in ACSF (in mM): 120 NaCl, 2 KCl, 1.2 NaH2PO4, 26 NaHCO3, 1.3 MgSO4, 1.6 CaCl2, 11 glucose, 2 ascorbic acid, 4 Na-lactic acid, 2 Na-pyruvate saturated with 95% O2-5% O2 at 300-320 mOsmol/L, pH 7.4, at 32ºC for 20 min followed by 1 h recovery and recordings at RT. Recorded signals were acquired at 100 kHz sampling rate and low pass filtered at 6 kHz. Cells were excluded from analysis if series resistance changed >20%.

Excitatory postsynaptic currents (EPSCs) were evoked (e) by a tungsten bipolar stimulating electrode placed in M1 L2/3 with stimulus intensities that yielded 40%-50% of the maximal response. AMPAR-eEPSC amplitudes were measured at the peak of the EPSC recorded at -70 mV holding potential. NMDAR-eEPSC amplitudes were recorded from the same neurons at +40 mV and measured at 40 ms after the stimulus artifact when AMPAR-eEPSCs have decayed.

Miniature EPSCs (mEPSCs) were recorded in whole-cell patch mode with 1 µM tetrodotoxin, 5 µM strychnine and 20 µM bicuculline methiodide (BMI) in the external solution. AMPAR-mEPSCs were recorded at -70 mV with 50 µM D-2-Amino-5-phosphonovaleric acid (D-AP5) to block NMDAR. NMDAR-mEPSCs were recorded at +45 mV with 5 µM Cyanquixaline (CNQX) to block AMPAR. Gamma-aminobutyric acid receptor and glycine receptor inhibitory postsynaptic currents (GABAR/GlyR-mIPSCs) were recorded at +15 mV with D-AP5 and CNQX. Amplitude and frequency of miniature events were detected using Mini-Analysis software (Synaptosoft, Decatur, GA) and inspected visually.

Paired-pulse stimulation was applied with interstimulus intervals (ISIs) of 35, 60, 100, 200 or 300 ms. The amplitude of the second eEPSC ($EPSC_2$), evoked by the second of the paired-pulse stimulations, was divided by $eEPSC_1$ amplitude to obtain a paired-pulse ratio (PPR). Long-term potentiation (LTP) of evoked EPSCs (recorded at -70 mV) was induced by theta-

burst stimulation (TBS, five trains of four pulses at 100 Hz in 200 ms intervals, repeated four times with an interval of 10 s) in the presence of 5 μM strychnine and 20 μM BMI.

Estimations of the readily releasable pool (RRP) size and synaptic vesicles (SVs) depletion rate were made from recordings of AMPAR-eEPSCs using high-frequency stimulation (HFS, 40Hz) trains of 15 pulses to deplete the RRP. Trains were analyzed to estimate glutamate probability of release (Pr) and RRP for each neuron using the decay method as previously described (54, 55) using OriginLab 10 software. RRP recovery was approximated as fractional recovery using initial train stimulation with interstimulus intervals of 0.1, 2, 5, and 10 s, followed by a single stimulus. Fractional recovery for each ISI was calculated as (eEPSCs2-eEPSCt1ss)/(eEPSCt1-eEPSCt1ss), where eEPSCs2-amplitude of the stimulus applied after the train, eEPSCt1-first amplitude of the train, eEPSCt1ss-steady state amplitude of the train (last 5 responses). 1 mM kynurenic acid was added to prevent AMPA receptor saturation; 50 μM vD-AP5 added to block NMDA receptors, 5 μM strychnine and 20 μM BMI to block GABA and glycine receptors.

PPR and train recordings for the rescue experiments were performed as described above with addition of 100μM NSC23766 into the recording solution with 5 min incubation period to allow for efficient slice penetration.

Quantitative Proteomics - Sample preparation

Cortices from male P21 mice (4 per genotype) was removed and immediately frozen in liquid nitrogen. Mouse brain tissues were transferred to Covaris tissueTUBE TT1 (Part No. 520001, Plug Part No. 520006), kept on dry ice, and flash frozen in liquid nitrogen prior to cryopulverization using a Covaris CP02 cryoPREP Automated Dry Pulverizer (Part No. 500001). The resulting powdered samples were transferred to 1.5 ml microcentrifuge tubes and lysed in 300 μl lysis buffer (8M urea in 50 mM Tris pH 8.0, 150 mM NaCl, 1 mM EDTA and protease phosphatase inhibitor) on ice. Lysates were sonicated using AFA Covaris E220 (Part No. 500239). The sonicated samples were centrifuged for 30 min at 10,000 rpm. Clear supernatants were transferred to new tubes and quantified with BCA assay (Thermo). Lysates were reduced with 10 mM TCEP and alkylated with 10 mM iodoacetamide for 30 min in the dark at room temperature. 1 mg lysates were diluted to 4 M urea with 200 mM Tris pH 8.0 and digested with Lys-C (1:50 protease:protein ratio) for 90 min at 37ºC. Samples were then diluted to less than 2 M urea with 200 mM Tris pH 8.0 and digested with trypsin at the same ratio overnight at 37º C. The samples were acidified with 1% formic acid and desalted using 50 mg per 1 cc Sep-Pak (Waters). A 250 μg aliquot of each sample was

frozen and dried, then stored at -80º C until tandem mass tag (TMTpro 16, Thermo lot# WI325918) peptide labeling according to manufacturer instructions.

Desalted 16-plex TMT labeled peptides (5 mg total) were subjected to basic reverse-phase (RP) chromatography. Peptides were separated using a 4.6 mm x 250 mm RP Zorbax 300 A Extend-C18 column (Agilent, 5 mm bead size) on an Agilent 1260 series HPLC. The 96 min gradient of solvent A (2% ACN, 5 mM ammonium formate) to solvent B (90% ACN, 5 mM ammonium formate) stayed at 0% B for 7 min, from 0% to 16% B over 6 min, from 16% to 40% over 60 min, from 40% to 44% over 4 min, from 44% to 60% over 5 min and maintained at 60% B over 14 min. Flow rate was 1 ml/min. 90 fractions were collected and concatenated to down to 24 fractions. 5% of each final fraction was used for proteome analysis. The remaining 95% of each of the 25 fractions were concatenated to 13 fractions. These 13 fractions were IMAC enriched using Ni-NTA Agarose beads as described for phosphoproteome analysis (56).

Quantitative Proteomics - Data acquisition

Proteome analysis was performed using an EASY-nLC 1200 UHPLC coupled to an Orbitrap Eclipse mass spectrometer (Thermo Fisher Scientific). The online peptide separation was performed using a 25 cm x 75 mm i.d. silica picofrit capillary column (New Objectives) packed with 1.9 mm ReproSil-Pur C18-AQ beads (Dr. Maisch GmbH). The 110 min method, 84 min effective gradient of solvent A (2% ACN, 0.1% FA) and solvent B (80% ACN, 0.1% FA). The gradient started at 2% B and increased to 10% B over 1 min, from 10% to 50% B over 84 min, from 50% to 72% B over 9 min, from 72% to 90% B over 1 min, stayed at 90% B over 5 min, then dropped to 60% B over 1 min and maintained at 60% B for 9 min. The flow rate was at 200 nl/min. The Eclipse mass spectrometer performed data-dependent acquisition in positive ion mode. MS1 spectra scanned a range of 350 – 2000 m/z at 60000 resolution, with maximum injection time of 50 ms and 100% AGC target. MS2 spectra scanned at first mass of 110 m/z at 50000 resolution. The cycle time for MS2 scan was set for 2 s for charge state of $1 < x < 6$, with isolation window of 0.7 m/z. The AGC target for MS2 was 60% with a maximum injection time of 105 ms. An empirically determined normalized collision energy was set to 32. Dynamic exclusion was set to 20 s.

Quantitative Proteomics - Data analysis

All .raw files were searched using Spectrum Mill (Agilent). MS2 spectra were searched against Uniprot Mouse Database (20171228, 47069 mouse entries, 264 common laboratory contaminants) with a mass tolerance of 20 ppm for both the precursor and product ions. The enzyme specificity was set for Trypsin and allowed up to three missed cleavages. The fixed

modification was carbamidomethylation at cysteine. TMT labeling was required at lysine, but peptide N-termini were allowed to be either labeled or unlabeled. Allowed variable modifications for whole proteome datasets were acetylation of protein N-termini, oxidized methionine, deamidation of asparagine, and pyroglutamic acid at peptide N-terminal glutamine, with a precursor MH+ shift range of -18 to 64 Da. The false discovery rate was less than 1%. Protein identifications were discarded if the protein was only observed by a single peptide. Protein subgroups were collapsed to the proteoform with the most evidence.

Gene Set Enrichment Analysis

Mouse UniProtIDs for identified proteins were converted to human orthologs and ranked by signed $\log_{10}$(nominal p-value) (with sign indicating direction of fold-change from WT). GSEA 4.3.3 (57, 58) was used to run the GSEA Preranked tests against all gene sets in the Human MSigDB Collection C2 v2023.2. SynGO 1.2 (59) was used to identify synaptic ontologies for differentially expressed proteins with nominal p-value <0.05.

Data Analysis

Statistical analyses were performed using GraphPad Prism 10. Data in bar graphs are presented as mean ± SEM, with individual data points graphed when applicable. Sample size ‘n’ is annotated within the bars or in the figure legend for each group. Distributions were tested for normality and outliers (>1.5x the interquartile distance for behavioral data, or by Prism ROUT method at Q = 5% for other metrics) were removed before proceeding with statistical tests. Specific details of statistical tests performed, adjusted with post-hoc Bonferroni test for multiple comparisons (MC) where appropriate, are included in the figure legends. Significance was defined by a p-value less than 0.05: ^{ns}p<0.1; *p<0.05; **p<0.01; ***p<0.001; ****p<0.0001.

RESULTS

Generation of *Trio* variant mice and impact on *Trio* isoforms

To evaluate how different ways of impairing Trio could affect mammalian brain development and function, we used CRISPR/Cas9 technology to generate mice bearing heterozygous *Trio* variant alleles in different Trio functional domains **(Fig. 1A,B)**. We chose these alleles for their discrete and measurable effects on TRIO levels or GEF activity in vitro: K1431M impairs TRIO GEF1 interaction with and subsequent activation of Rac1 in vitro up to 8-fold **(Supp. Fig. 1A,B)** (23, 28), M2145T TRIO GEF2 has a reduced ability to activate RhoA as a function of protein concentration in cells (23), and K1918X is predicted to lead to nonsense-mediated decay and loss of Trio protein (23). These *Trio* variant alleles are found heterozygous in individuals with NDDs: *+/K1431M* is associated with ASD, *+/K1918X* is associated with SCZ, and *+/M2145T* is a *de novo* mutation found in an individual with BPD (60).

Because *Trio* knockout mice exhibit decreased survival (15-17), we first verified the viability of mice bearing these CRISPR/Cas9-generated *Trio* alleles. Mice heterozygous for any one of these three *Trio* alleles survived to adulthood. Mice homozygous for *Trio K1431M* and *M2145T* survived to adulthood, with genotypes from offspring of *+/K1431M* intercrosses observed in Mendelian ratios, but fewer than expected *M2145T* homozygotes obtained from *+/M2145T* intercrosses **(Supp. Fig. 1C)**. *K1918X* homozygote pups were not observed **(Supp. Fig. 1C)**, as expected for a *Trio* null allele (15, 17). We focused on heterozygotes, as most rare damaging *Trio* variants are heterozygous in humans.

Alternative splicing of the full-length *TRIO* transcript generates multiple brain-specific isoforms of various sizes, whose expression level varies by brain region and developmental age: cortex-predominant Trio9S (263 kDa) and Trio9L (277 kDa), brain-wide Duet (145 kDa), and cerebellum-specific Trio8 (217 kDa) **(Fig. 1A)** (61, 62). Heterozygosity for the *K1431M* and *M2145T* alleles did not alter the levels of the predominant Trio isoforms in the brain at postnatal day 0 (P0, neonate) **(Fig. 1C-D)** or at P42 (young adult) **(Supp. Fig. 1D-L)**. Trio9 protein levels were reduced by ~50% in the brains of *+/K1918X* mice at P0 **(Fig. 1C-D)** and P42 **(Supp. Fig. 1D-L)**, and we did not detect the presence of residual truncated protein (expected at 217 kDa), suggesting this *K1918X* mutation indeed leads to nonsense-mediated decay as predicted. Meanwhile, as the *K1918* site is not contained in these isoforms, the levels of Trio8 and Duet were unaffected **(Supp. Fig. 1D-L)**.

***Trio* variant alleles differentially impact active Rho family GTPase levels.**

Having demonstrated that heterozygosity for the K1431M and M2145T alleles does not alter Trio protein levels in the brain, we can attribute any observed differences to the effects of these missense mutations on Trio GEF domain function rather than changes in Trio protein expression. Given the effects of these variants on TRIO GEF1/2 activities in vitro, we measured levels of active GTP-bound Rac1 and RhoA in brains of neonatal (P0) and young adult (P42) *Trio* variant-bearing mice **(Fig. 1E-H)**.

In concordance with the ~50% reduction in Trio levels in *+/K1918X* brains **(Fig. 1C,D)**, Rac1 activity was decreased in P0 *+/K1918X* brains (91% of WT activity, $p<0.05$) **(Fig. 1E)**, with a trend toward decreased active RhoA levels (84% of WT, $p=0.0865$) **(Fig. 1F)**. However, by P42, *+/K1918X* brains did not differ from WT in Rac1 or RhoA activity **(Fig. 1G,H)**, despite the persistent ~50% reduction in Trio9 protein level at this age **(Supp. Fig. 1D-F,H-J)**.

As K1431M decreases TRIO GEF1 catalytic activity in vitro **(Supp. Fig. 1A,B)** (19, 23, 28), we anticipated Rac1 activity would also be reduced in *+/K1431M* mice. Instead, active Rac1 levels were significantly elevated in *+/K1431M* whole brain lysates compared to WT controls, showing a 111% increase at P0 ($p<0.01$) **(Fig. 1E)** and an even greater increase of 150% at P42 ($p<0.05$) **(Fig. 1G)**. Despite evidence of M2145T impacting TRIO GEF2 catalytic activity in vitro (23), we did not detect changes in active RhoA levels at the whole brain lysate level in *+/M2145T* mice at either age **(Fig. 1F,H)**.

Because Trio, Rac1, and RhoA are enriched at synapses (14, 21, 23, 63), we also measured GTPase activities in synaptosomes **(Supp. Fig. 1M-P)**, within the same age range as the electrophysiological recordings performed on these mice. Active Rac1 was significantly increased in *+/K1431M* crude synaptosomes from P42 cortex (112% of WT, $p<0.01$) **(Fig. 1I)**, consistent with our findings in *+/K1431M* whole brain lysates **(Fig. 1E,G)**. We also measured decreased levels of active RhoA in P42 *+/M2145T* cortical synaptosomes compared to WT (73% of WT, $p<0.01$) **(Fig. 1J)**, consistent with its reduced GEF2 activity in vitro (23) **(Fig. 1F,H)**.

Distinct Trio variants differentially impact mouse behavior.

NDDs affect learning and memory, compulsivity, motor coordination, and social skills, hence we assessed these skills using a diverse array of established behavioral tests (18) in P42 mice bearing *Trio* variants **(Fig. 2A)**.

We measured motor coordination and learning using an accelerating rotarod test. *+/K1431M* and *+/K1918X* mice of both sexes fell from an accelerating rotarod with reduced latency

relative to WT littermates, while *+/M2145T* mice performed similarly to WT **(Fig. 2B)**. In addition, *+/K1431M* and *+/K1918X* males and *+/K1431M* females showed a lower rate of improvement in this skill over repeated trials **(Fig. 2B)**. No deficits in muscle strength were noted in any genotype using the Kondziela inverted screen test prior to rotarod testing.

We used an open field test (OFT) and the elevated plus maze (EPM) to assess general locomotor activity and exploratory behavior. In the OFT **(Supp. Fig. 2A-D)**, *Trio* variant mice did not differ significantly from WT in total distance traveled or mean speed; however, *+/K1431M* females spent a greater amount of time in the outer and corner zones of the OFT compared to WT **(Supp. Fig. 2D**, *right***)**, suggesting increased anxiety-like behavior in *+/K1431M* female mice. WT mice prefer the protected closed arms over the open arms in the EPM **(Supp. Fig. 2E,F)**, whereas *+/K1431M* and *+/K1918X* mice of both sexes and *+/M2145T* females did not exhibit this preference **(Supp. Fig. 2F)**.

Deficits in social communication and social interaction are defining features of individuals diagnosed with NDDs (1). In a three-chamber social interaction test, *+/K1431M* mice of both sexes and *+/K1918X* females showed no preference for the stranger mouse over the object **(Fig. 2C)**, while *+/M2145T* mice of both sexes and *+/K1918X* males exhibited preference for the stranger mouse, similar to WT **(Fig. 2C)**. In a novel object recognition test, *+/K1918X* mice of both sexes and *+/M2145T* females failed to discriminate between the novel and familiar objects, while *+/K1431M* mice and *+/M2145T* males exhibited normal discrimination between novel and familiar objects similar to WT **(Fig. 2D)**.

Repetitive behaviors and stereotypies are often identified in individuals with NDDs (64). We found a significant increase in compulsive nestled shredding in *+/K1918X* and *+/K1431M* males, with no significant changes in females **(Fig. 2E**).

Behavioral phenotypes mostly overlapped between *+/K1431M* and *+/K1918X* mice, with differences in social interaction and memory tests. *+/M2145T* mice exhibited the fewest phenotypes in measured tasks. Additionally, some behavioral manifestations appeared to be selective to one sex. Together, these data indicate that these *Trio* alleles differentially impact behavior.

***Trio +/K1431M* and *+/K1918X* mice have smaller brains.**

TRIO variants that reduce TRIO GEF1 activity are associated with microcephaly (24, 25, 32), so we assessed head and brain size in *Trio* variant mice **(Fig. 3A-E** (males), **Supp. Fig. 3A-E** (females)**)**. After adjusting for body weight, both the head width **(Fig. 3D**, **Supp. Fig. 3D)** and brain weight **(Fig. 3E**, **Supp. Fig. 3E)** were reduced in P42 adult *+/K1431M* mice of both

sexes relative to WT, consistent with the microcephaly seen in patients harboring *TRIO* GEF1-deficient alleles. Of note, these ratios were driven by the increased body weight exhibited by P42 *+/K1431M* mice of both sexes compared to WT counterparts **(Fig. 3C**, **Supp. Fig. 3C)**. *+/K1918X* mice of both sexes displayed a reduced brain weight-to-body weight ratio **(Fig. 3E**, **Supp. Fig. 3E)** but an unchanged head width-to-body weight ratio **(Fig. 3D**, **Supp. Fig 3D)** relative to WT, suggesting a disproportionate reduction in brain mass in *+/K1918X* mice. Meanwhile, *+/M2145T* mice did not differ from WT in either head width or brain weight when adjusted for body weight.

***Trio* variant mice show mild changes in cortical organization.**

We examined whether the decreased brain weight and head size observed in *+/K1431M* and *+/K1918X* mice were associated with anatomical defects. Gross histological analyses of fixed Nissl-stained brain sections in P42 male mice showed only mild morphological defects **(Fig. 3F-J)**. We observed reductions in both total cross-sectional brain area **(Fig. 3F-G)** and cortical thickness **(Fig. 3H-I)** in *+/K1918X* brains, consistent with their smaller head size and brain weight. Significant decreases in cortical layer 2/3 and layer 5 thickness were observed in *+/K1918X* brains **(Fig. 3H-J)**, and were in proportion to the relative decrease in cortical thickness relative to WT **(Supp. Fig. 3F)**. Meanwhile, no significant differences in brain area or cortical thickness were observed in either *+/K1431M* or *+/M2145T* mice.

Deletion of *Trio* has been shown to impair the migration of forebrain interneuron progenitors, resulting in fewer neurons entering the cerebral cortex and altered distribution of cortical layers (19, 65). However, we observed no change in total cortical cell density or in layer-specific cell density in heterozygous *Trio* variant male mice, nor were numbers of cortical NeuN+ neuronal cells or PV+ inhibitory neurons altered relative to WT, although there were trends toward increased DAPI+ cell density in *+/K1918X* and increased NeuN+ cell density in *+/M2145T* motor cortex **(Supp. Fig. 3H-N)**. These data suggest that the reduced brain size of *+/K1918X* mice results from a loss of neuropil rather than reductions in cortical neuron number.

Trio variant heterozygotes exhibit alterations in dendritic arbors and synaptic ultrastructure.

Altered dendritic arbor morphology and dendritic spine abnormalities are hallmarks of NDDs (66-72). Excitatory neuron-specific ablation of one or both *Trio* alleles decreased dendritic arborization, increased spine density, and yielded smaller synapses in cortex area M1 Layer 5 pyramidal neurons (M1 L5 PNs) (18).

Sholl analysis of M1 L5 PNs revealed significant reductions in both basal and apical dendritic arbor complexity and dendritic field size in P42 *+/K1918X* neurons, an increase in proximal basal arbor complexity in *+/K1431M* neurons, and a decrease in distal apical arbor complexity and apical dendritic field size in *+/M2145T* neurons relative to WT **(Fig. 3K-O**, **Supp Fig. 3.G)**

Conditional *Trio* knockout specifically in forebrain excitatory neurons significantly increased the dendritic spine density on M1 L5 PNs, although they were smaller and appeared more immature (18). Notably, none of the *Trio* variant heterozygotes exhibited altered dendritic spine density on M1 L5 pyramidal neurons compared to WT mice on either apical or basal secondary arbors **(Supp. Fig. 4L,M**).

Electron microscopy of cortical area M1 L5 revealed that synapse density was significantly increased in *+/K1918X* mice compared to WT **(Fig. 4A,B)**, possibly due to a net reduction in neuropil resulting from smaller dendritic arbors. Within synapses, postsynaptic density (PSD) length was slightly decreased in *+/K1918X* (by 6%) and *+/M2145T* (by 6.6%) mice relative to WT, but not in *+/K1431M* mice **(Fig. 4C)**. Cross-sectional presynaptic bouton area and spine head area were similar to WT in each *Trio* variant heterozygote **(Fig. 4D,E)**.

Synaptic vesicle (SV) distribution was significantly altered in *+/M2145T* mice relative to the other genotypes **(Fig. 4F,G)**. The densities of both docked and tethered vesicles at 15 and 50 nm from the active zone (AZ) respectively, which together can estimate the readily releasable pool (RRP) (52, 53), were significantly increased in *+/M2145T* relative to the other genotypes **(Fig. 4F,G)**. Also, SV distribution at 200 nm from the AZ, thought to contribute the reserve pool, were also significantly increased in *+/M2145T* mice, suggesting an overall larger SV pool size. No differences in synaptic vesicle distribution were noted in *+/K1431M* mice, while *+/K1918X* showed modestly increased SVs at 200 nm from AZ relative to WT.

Synaptic transmission and plasticity are differentially impaired by distinct *Trio* variants.

Loss of Trio function or disruption of TRIO GEF1 activity in slice culture decreases AMPAR levels at excitatory synapses (18, 20, 21, 28), while mice bearing a GEF1-deficient *Trio* allele exhibited decreased gamma-aminobutyric acid receptor (GABAR)- and glycine receptor (GlyR)-mediated inhibitory miniature current (mIPSC) frequencies in the prefrontal cortex (19). To explore how *Trio* variants impact synaptic function, we measured both miniature excitatory currents (mEPSCs) and mIPSCs in M1 L5 PNs in each of the *Trio* variant heterozygotes at P35-42 consistent with other experiments.

AMPAR-mediated mEPSC amplitudes were significantly increased in *+/K1431M* and *+/K1918X* mice relative to WT littermates, with no change in their frequencies **(Fig. 5A-C)**. In contrast, AMPAR-mediated mEPSC amplitudes were unchanged in *+/M2145T* mice, but their frequencies were significantly increased. No significant changes in NMDAR mEPSC amplitudes were noted, while NMDAR mEPSC frequencies were decreased in *+/K1431M* and increased in *+/M2145T* mice cortex **(Fig. 5D-F)**. Notably, these findings correlated with gross alterations in the ratio of NMDAR/AMPAR-mediated evoked (e)EPSCs measured in M1 L5 PNs following stimulation in L2/3. *+/K1431M* and *+/K1918X Trio* variant heterozygotes showed decreased NMDA/AMPA ratios, indicating imbalances in NMDAR- versus AMPAR-mediated conductance **(Fig. 5J,K)** and suggesting an increase in synaptic AMPAR signaling in both mice. Significant decreases in mIPSC frequencies were noted in *+/K1431M* and *+/M2145T* mice relative to WT mice, with no change in amplitudes **(Fig. 5G-I)**. *+/K1918X* mice exhibited increased mIPSC amplitude with no observed change in mIPSC frequency. Together, these data indicate that the *Trio* variants differentially impact excitatory and inhibitory transmission.

Finally, we tested the ability of the L5 PNs to undergo long-term potentiation (LTP) following theta-burst stimulation of L2/3 afferents **(Fig. 5L,M)**. While LTP was robustly induced and potentiated in M1 L5 PNs from WT mice, LTP induction and potentiation were deficient in slices from *+/K1918X* and *+/K1431M* mutant mice. In contrast, *+/M2145T* L5 PNs showed increased induction and prolonged potentiation of LTP compared to WT L5 PNs.

Neurotransmitter release is altered in *Trio +/K1431M* and *+/M2145T* heterozygotes.

In addition to its postsynaptic roles, Trio localizes presynaptically and interacts with the presynaptic active zone scaffolding proteins Bassoon and Piccolo (13, 14, 21). Additionally, recent work demonstrates that Rac1 activity levels can bidirectionally affect SV probability of release (Pr) in excitatory synapses (14, 56, 80). To assess the impact of *Trio* variants on presynaptic function, we first measured the paired-pulse ratio (PPR) to test possible changes in Pr. Synapses with a low probability of release (Pr), such as L2/3 onto L5 PNs synapses, exhibit paired-pulse facilitation (PPF), where synaptic response increases for the second of two apposed stimuli due to elevated residual Ca^{2+} promoting SV fusion. WT and *+/K1918X* M1 L5 PNs exhibited normal facilitation of eEPSC amplitudes that decreased with increased interstimulus interval (ISI) **(Fig. 6A,B)**. PPF was significantly enhanced in *+/K1431M* M1 L5 PNs at short ISIs relative to WT, suggesting a reduction in Pr at these synapses **(Fig. 6A,B).** The *+/M2145T* PPR curve was complex, with significantly reduced PPF at short ISIs, yet clearly increased PPF at longer ISIs compared to WT **(Fig. 6A,B)**. The decreased PPF at initial ISIs in *+/M2145T* mice, together with an increase in both AMPAR and NMDAR

mEPSC frequency **(Fig. 5A-C)**, demonstrate an increase in both synchronous and spontaneous glutamate Pr.

To further characterize changes in neurotransmitter release in these mice we used high frequency (40Hz) stimulation (HFS) trains to quantitatively estimate glutamate Pr, RRP size, and rates of SV depletion and recovery. A plot of the normalized eEPSC responses to a HFS train stimulation again revealed facilitation upon the first 2-3 stimulations that was increased in *+/K1431M* and decreased in *+/M2145T* slices relative to WT, with no changes in *+/K1918X* slices (**Fig. 6C,D**). Initial facilitation was followed by decaying eEPSC amplitudes, reflecting SV depletion under HFS. *+/K1431M* and *+/M2145T Trio* variants exhibited a slower train decay rate relative to WT during HFS with *+/M2145T* depleting at half the rate of WT (τ_d, *+/K1431M:* 3.19 s, *+/M2145T:* 4.79 s vs WT: 2.70 s) **(Fig. 6D)**.

We used a 'Decay' method (54, 55) to estimate Pr and RRP size from HFS trains which allows us to account for initial facilitation seen in the train eEPSCs. Glutamate Pr in the L2/3-L5 synapses was increased in *+/M2145T* mice, while it was decreased for *+/K1431M* mice **(Fig. 6E)**, consistent with the relative changes observed in PPF for these mice. RRP size was much larger in L2/3-L5 synapses of *+/M2145T* mice relative to WT **(Fig. 6F)**, consistent with the increased SV distribution found at 15-50 nm from the AZ in electron micrographs **(Fig. 4F,G)**. We tested the ability of *Trio* variant heterozygotes to recover after train depletion by pairing HFS train with a single stimulus at increasing intervals (0.01, 2, 6, 9, 12, 18s) and calculating the fractional recovery (see Methods). The recovery rate (τ_R) was significantly slower in *+/K1431M* L5 PNs and they did not recover to their initial strength within 18s, plateauing at 78% of maximal recovery compared to WT **(Fig. 6G)**. Together, *Trio +/K1431M* and *+/M2145T* mice exhibit distinct and significant alterations in short-term plasticity and synchronous glutamate release.

Trio variant cortex displays different proteomic signatures

We used comparative proteomics from P21 cortex to identify proteins and pathways that were differentially altered by the *Trio* variants. We quantified a total of 7,362 proteins, finding distinct differences in the cortical proteome for each genotype **(Supp. Fig. 5, Supp. Table 1)**. Gene Set Enrichment Analysis (GSEA) (57, 58) revealed alterations in distinct functions for each *Trio* variant **(Fig. 7A; Figure 7 - Source data 1)**. Of note, the only enriched gene set specific to neurons was downregulation of the synaptic vesicle pathway in *+/K1431M* cortex; all other gene sets were not cell type-specific.

We used SynGo (59) to investigate whether the *Trio* variants impacted synaptic functions. 1,067 of the 7,362 total quantified proteins were synaptic proteins listed in the SynGO

geneset **(Figure 7, Figure 7 - Source data 2)**. When restricted to brain-specific genes, all three *Trio* variant heterozygotes showed enrichment of differentially expressed proteins (DEPs) in synaptic processes **(Fig. 7B,C)**. Notably, *+/M2145T* upregulated DEPs and *+/K1431M* downregulated DEPs were significantly enriched at the presynapse **(Fig. 7B)**, but with only *+/K1431M* downregulated DEPs showing significant enrichment for postsynaptic receptor and synaptic vesicle cycling **(Fig. 7C)**. Meanwhile, *+/K1918X* showed enrichment of DEPs at the postsynapse, particularly in the postsynaptic density **(Fig. 7B)**. Together, our proteomics data point to a significant deficit in presynaptic function in both *+/K1431M* and *+/M2145T* cortex, as well as a significant effect of *+/K1431M* on postsynaptic function.

Rho GEFs and synaptic regulatory proteins are altered in *Trio +/K1431M* and *+/M2145T* heterozygotes.

Given our findings from proteomic analysis and electrophysiology, we measured levels of key presynaptic regulators, including synaptophysin (Syp), syntaxin binding protein1 (Stxbp1, also known as Munc18-1), syntaxin1a (Stx1a) and synaptotagmin3 (Syt3), which are crucial for synaptic vesicle (SV) tethering, docking, replenishment, and calcium-dependent replenishment, respectively. We also measured levels of presynaptic proteins in P42 cortical synaptosomes, where these proteins are enriched. Munc18-1, Syt3, and Syp levels were increased in *+/M2145T* synaptosomes relative to WT **(Fig. 7D-H)**. Meanwhile, Stx1a levels were significantly decreased in *+/K1431M* synaptosomes compared to WT, with no significant changes in *+/K1918X* compared to WT mice.

The elevated Rac1 activity in *+/K1431M* brain lysates and synaptosomes **(Fig. 1I)** seemed at odds with previous reports that K1431M reduces TRIO GEF1 activity **(Supp. Fig. 1A,B)** (19, 23, 28). We hypothesized that homeostatic compensation in *+/K1431M* mice may alter expression of other RhoGEFs and GAPs. Indeed, levels of the Rac1 GEF Tiam1 were increased in both *+/K1431M* and *+/M2145T* P42 cortical lysates, while VAV2 levels were increased in *+/M2145T* P42 lysates **(Fig. 7I-L)**. Levels of the Trio paralog Kalirin (73) were unaffected in the *Trio* variant mice at P42 **(Fig. 7J)**. Together, our proteomic analyses suggest that presynaptic functions are altered in *+/K1431M* and *+/M2145T* mice and may be driven by abnormal levels of crucial presynaptic regulatory proteins and changes in Rac1 and RhoA activity.

NSC23766, a Rac1-specific inhibitor, rescues neurotransmitter release in *Trio +/K1431M* heterozygotes.

Rac1 negatively regulates synaptic vesicle replenishment and synaptic strength in excitatory synapses (14, 74). In *+/K1431M* synapses, increased Rac1 activity and decreased Stx1a

levels were associated with reduced synaptic strength and impaired vesicle replenishment. We tested if the acute application of the Rac1 inhibitor NSC23766 (NSC) could rescue these deficits. Treatment of *+/K1431M* and WT slices acutely with NSC shifted the PPF downwards in M1 L5 PNs, suggesting an increase in Pr in both cases **(Fig. 8A,B)**. Notably, at longer ISI, PPRs in NSC-treated WT slices still normalized at around 1, while PPRs in NSC-treated *+/K1431M* slices shifted below 1, exhibiting slight depression.

Application of NSC to WT and *+/K1431M* slices under HFS train stimulation decreased initial facilitation in both **(Fig. 8C,D)**, and significantly increased Pr **(Fig. 8E)** without affecting RRP size **(Fig. 8F)** in both, rescuing the initial Pr in *+/K1431M* slices **(Fig. 8C-F)**. NSC treatment also led to a faster train decay rate (τ_d) in *+/K1431M* slices but did not significantly change WT relative to untreated slices (*+/K1431M* +NSC τ_d, 2.66 s vs. initial 3.19 s; WT +NSC: 2.85 vs. 2.70 s) **(Fig. 8D)**.

Finally, we tested if acute Rac1 inhibition impacts the rate of recovery of the RRP following HFS stimulation. NSC treatment increased the fractional recovery rate (τ_R) in both WT and *+/K1431M* slices (WT +NSC: 32% faster than WT; *+/K1431M* +NSC: 40% faster than *+/K1431M*). NSC treatment of *the +/K1431M* variant allowed for full recovery at 18s interval and sped up the recovery rate, but it remained significantly slower compared to WT (by 45%) **(Fig. 8G).**

Overall, we demonstrate that presynaptic Trio GEF1-dependent Rac1 signaling is crucial for maintaining synchronous glutamate Pr and SV replenishment at cortical L2/3-L5 synapses.

DISCUSSION

Large-scale genetic studies show significant overlap in risk genes for ASD, SCZ, and BPD, many converging on synaptic proteins (75-83). However, how variants in a single gene contribute to different NDDs remains a major unresolved question. Our study reveals that mice heterozygous for NDD-associated *Trio* variants differentially affecting Trio protein levels or GEF activity yield overlapping but distinct behavioral, neuroanatomical, and synaptic phenotypes. Our findings extend prior work demonstrating that Trio is critical for postsynaptic signaling and synaptic plasticity. We also demonstrate for the first time in mice that Trio is critical for glutamate release and synaptic vesicle recycling, and that NDD-associated variants differentially impact these pre- and post-synaptic roles.

Heterozygosity for *Trio* variants in mice yields phenotypes similar to those observed in NDDs.

Individuals with mutations in *TRIO* present with a range of neurodevelopmental disorder-associated clinical features, including varying degrees of intellectual disability, altered head size, skeletal and facial features, and behavioral abnormalities (22, 24-27, 32, 84). Patients with missense or truncating variants in *TRIO* that reduce GEF1 activity have mild developmental delay and microcephaly (24, 25, 27, 32). Similarly, we found that heterozygosity for the GEF1-deficient *K1431M* missense or the *K1918X* nonsense variants significantly reduced brain weight and/or head size compared to WT mice, along with multiple behavioral impairments. Notably, while both showed impaired motor coordination and learning, only mice bearing the ASD-associated *K1431M* allele exhibited social interaction deficits. In addition, we observed behavioral differences in male versus female *Trio* variant mice, possibly similar to human sex differences in the susceptibility to and clinical presentation of NDDs (85).

Both *+/K1431M* and *+/K1918X* adult mice of both sexes had reduced brain-to-body weight ratios compared to WT, but these were driven by different factors. The smaller brain size in *+/K1918X* male mice was associated with a reduction in neuropil and reduced cortical thickness, similar to mice bearing excitatory neuron-specific ablation of one *Trio* allele (18) and paralleling the reduced gray matter volume and cortical thickness in SCZ patients (86-90). Meanwhile, *+/K1431M* mice of both sexes exhibited an overall increase in body weight leading to relatively decreased head width- and brain-to-body weight ratios in these mice. Adult *+/K1431M* male mice had no change in neuropil or cross-sectional brain area, consistent with a prior study describing normal brain size in *+/K1431M* at E14.5 (19). Rac1 mediates glucose-stimulated insulin secretion from pancreatic islet beta-cells (91-96), which may explain how chronic alterations in Rac1 activity contribute to weight changes in *Trio*

+/K1431M and *+/K1918X* mice. Most studies of *Trio* variants have focused on neuronal effects, but expression of *Trio* in other tissues could explain the increased body weight in these mice, as well as the musculoskeletal abnormalities associated with *TRIO* variation in humans (22, 24, 26, 31).

Trio variants differentially impact dendritic arbor structure.

Rac1 and RhoA signaling is critical for dendrite development (9-12, 97). We found relatively subtle effects of Rac1/RhoA-altering *Trio* variants on cortical L5 PN dendrites. *+/K1918X* L5 pyramidal neurons are smaller and less complex than WT neurons, especially in the basal compartment corresponding to L5 where EM images were obtained, consistent with the smaller brain size and reduced cortical thickness of *+/K1918X* mice. We posit that due to their smaller dendritic field size, L5 neurons pack more densely, contributing to the mildly increased synapse density observed in *+/K1918X* M1 L5 cortex. Consistent with this hypothesis, we observed a trend toward increased DAPI+ cell density in M1 L5 of *+/K1918X* neurons.

The reductions in dendritic arborization and length in *+/K1918X* neurons are consistent with reports of reduced gray matter volume and dendrite alterations in individuals with schizophrenia versus controls (98, 99), but were modest compared to *NEX-Trio*$^{+/fl}$ mice lacking one copy of Trio in excitatory neurons (18). Reduced Trio function in other cell types, such as in inhibitory neurons or glia, or in neurons from other brain regions that project to cortical M1 L5 PNs, may ameliorate the phenotypes in excitatory neurons of *+/K1918X* relative to *NEX-Trio*$^{+/fl}$ mice. In addition, changes to L5 PN dendrites in *Trio* variant mice appeared to be regionally selective within the arbor: *+/K1431M* neurons had increased arborization only in proximal basal dendrites, while *+/M2145T* neurons had decreased arborization only in the most distal apical dendrites. These differences may reflect the differential spatiotemporal influence of Trio in regulating Rac1 versus RhoA activity. Alternatively, given our finding for presynaptic roles for Trio, these differences may reflect differential effects of the *Trio* variants on both excitatory and inhibitory afferent synaptic inputs which play critical roles in shaping the apical and basal dendrites of L5 PNs (100).

Trio variants impact brain Rho GTPase signaling.

We show here that the *K1431M* variant significantly reduces TRIO GEF1 nucleotide exchange on Rac1 in vitro, consistent with previous reports (23, 28). Decreased Rac1 activity was observed in +/*K1431M* mice at embryonic day 14.5 in the ganglionic eminence, which is enriched for pre-migratory GABAergic interneurons (19). In contrast, we show an increase in active Rac1 levels in *+/K1431M* postnatal brains (at P0, P21, P42) and

synaptosomes (at P42) from cortex, primarily composed of differentiated excitatory neurons. This increase aligns with observed phenotypes (e.g. reduced Pr) and reveals why reductions in brain volume, dendrites and spines, or AMPAR signaling anticipated from reduced Rac1 activity (101-105) were not observed in *+/K1431M* mice**.** We propose that the increased Rac1 activity we observed reflects homeostatic compensation in Rac1 regulation occurring between birth to adult ages, and identify changes in Rac1-specific GEFs, e.g. Tiam1 and Vav2, that may contribute to this compensation. Importantly, we did not find changes in Kalirin levels in the adult brain of these Trio mutant mice, suggesting that Kalirin does not compensate for loss of Trio GEF1 activity at this age.

We observed a significant reduction in active RhoA only in purified synaptosomes of *+/M2145T* brains, reflecting the synaptic compartment as a key locus of Trio function. In addition, despite *+/K1918X* mice having half the WT levels of Trio protein, we measured little to no change in active Rac1 and RhoA levels in *+/K1918X* brains. These findings are consistent with recent evidence that the spatiotemporally precise balance of Rac/Rho activity rather than absolute activity levels can mediate cytoskeletal rearrangements (6, 8, 106, 107). Alterations in the activity of additional potential TRIO substrates, such as RhoG (108), Cdc42 (5), and the neurodevelopmentally critical Rac3 (109-111) could also contribute phenotypes in these mice.

Our results strongly complement a growing body of evidence showing that altered activation of Rho GTPases is an important mechanism affecting synaptic function in ASD (85, 112-116). This highlights Rho GTPase signaling as a convergent pathway in ASD and therefore an attractive target for pharmacotherapy for these disorders.

The NDD-associated *Trio* variants cause synaptic transmission, plasticity and excitatory/inhibitory imbalance.

Overexpression of a TRIO *K1431M* variant with reduced GEF1 activity decreased AMPAR-mediated mESPC amplitudes in rat organotypic slices (20), while Rac1 activation increased AMPAR amplitudes by promoting synaptic AMPAR clustering (105, 117). In *+/K1431M* mice, we observed a decrease in the NMDA/AMPA ratio and NMDA mEPSCs frequency, with increased AMPAR mEPSCs amplitudes, with no changes in dendritic spines suggesting a possible reduction in silent synapses due to increased AMPAR incorporation. This increase in AMPAR was associated with increased active Rac1 levels measured in synaptosomes in adult *+/K1431M* mice. AMPAR mEPSC amplitudes were also increased in L5 PNs of *+/K1918X* mice, corresponding with a decrease in the NMDA/AMPAR ratio, but no changes in mEPSCs frequencies, also suggesting an increased number of synaptic AMPARs. In

+/K1918X cortex, Rac1 activity is reduced at P0 but increases by P21 and P42 to WT levels, suggesting that a *relative* increase in Rac1 during development may enhance AMPAR tone and affect LTP, especially given the precise spatiotemporal requirements of Rac/Rho activity and their effectors for LTP (105, 117-120). The *+/M2145T* variant showed no changes in AMPAR or NMDAR amplitudes but had increased mEPSC frequencies in both, without changes in spine or synapse density, consistent with enhanced spontaneous neurotransmitter release.

mIPSC frequencies were decreased in *+/K1431M* and *+/M2145T* L5 PNs, while mIPSC amplitude was increased in *+/K1918X* slices. Sun et al. noted a similar deficit in inhibitory function in *+/K1431M* prefrontal cortex correlated with reduced interneuron migration to this region, including parvalbumin positive (PV+) neurons (19). In contrast, we did not observe reduced PV+ interneuron numbers in the motor cortex in any *Trio* variant mice, suggesting that *Trio* variants may also impact the number of inhibitory synapses or transmission. However, we cannot fully exclude potential defects in migration of other interneuron populations as contributors to these phenotypes.

Overall, heterozygosity for *Trio* variants dysregulates excitatory and inhibitory synaptic transmission in different patterns, resulting in E/I imbalance, a known driver of NDD phenotypes.

Trio-deficient excitatory neurons are unable to undergo long-term potentiation (LTP) in mouse brain slices (18), which is crucial for working memory in mammals. During LTP, Rac1 is suggested to be transiently activated and deactivated to regulate AMPAR (105, 117-120). Both *+/K1431M* and *+/K1918X* L5 PNs exhibited reduced LTP induction and maintenance. The increased AMPAR resulting from elevated Rac1 activity (*+/K1431M* mice) or the inability of reduced levels of Trio to activate Rac1 (*+/K1918X* mice) may preclude LTP in these mice. *+/M2145T* mice showed a striking increase in the induction and maintenance of LTP, correlating with an increased glutamate Pr and SV pool size. The function of RhoA in plasticity is unknown, but the decrease in RhoA activity and increased levels in presynaptic machinery proteins measured in cortical synaptosomes may underlie the increase in LTP in these mice.

Trio GEF1 and GEF2-deficient variants lead to opposing defects in the synaptic release of glutamate.

In neuroendocrine, pancreatic beta, and mast cells, Trio GEF1 activity, Rac1 and RhoA are required for regulation of exocytosis (121-125). Recent work suggests that Trio GEF1 can act through Rac1 to regulate presynaptic processes – Rac1 colocalizes with SVs in the

axonal boutons to negatively regulate action potential-dependent (synchronous) glutamate Pr and SV replenishment (14, 74, 126, 127). Using the Rac1 inhibitor NSC, we demonstrate that elevated Rac1 activity, potentially driven by Tiam1 upregulation, drives the reduction in synchronous glutamate Pr and SV replenishment without affecting RRP in *+/K1431M* mice. NSC application rescues Pr and enhances SV replenishment in *+/K1431M* slices while also increasing both processes in WT. Decreased Stx1 levels in *+/K1431M* synapses, a key component of the priming machinery, may still be a limiting factor in effective priming, thus preventing full rescue of the SV recovery by NSC. Overall, NSC had a significant yet weaker effect in WT than in *+/K1431M* slices, likely due to the overall increased Rac1 activity in *+/K1431M* slices providing more of a target for NSC.

Conditional knock out of Rac1 in the Calyx of Held increased spontaneous (action potential-independent) glutamate Pr (74), aligning with the hypothesis that Rac1 activity negatively regulates neurotransmitter release by increasing the assembly of actin filaments at the AZ that impede SV fusion. *+/K1431M* cortical slices showed significant increases in AMPAR amplitudes, and our data are consistent with fewer silent synapses. Yet, we observed no change in AMPA mESPC frequency. We hypothesize that the Rac1-dependent decrease in Pr identified in these slices decreased AMPAR mEPSCs frequency; hence, the opposing changes from these pre- and post-synaptic effects mask the expected change in AMPAR mEPSC frequency.

RhoA activity is significantly reduced in cortical synaptosomes of *+/M2145T* mice, and this is associated with increased RRP size. While a specific function for RhoA in regulating presynaptic release is currently unclear, levels of Munc18, Syp, and Syt3, are all increased in *+/M2145T* mice at P42 and can contribute to the enhanced Pr and altered SV cycling. The unusual PPR in the *+/M2145T* variant may result, at least in part, from altered Syt3 levels, crucial for calcium-dependent SV replenishment, as its deficiency causes similar phenotypes (128).

Our findings show that Trio GEF1 and GEF2-mediated Rho GTPase signaling pathways play critical and distinct roles in regulating Pr, RRP size and SV recycling.

Conclusions

TRIO is a risk gene for several NDDs with different patterns of variants observed in different disorders. We show here that variants in *Trio* that lead to impaired Trio levels or GEF function cause both shared and distinct defects in behavior, neuroanatomy, and prominent synaptic dysfunction that may reflect variant-specific NDD clinical phenotypes. Our data also

demonstrate, for the first time, the differential impact of distinct *Trio* lesions on glutamate Pr, RRP size, and SVs replenishment, along with alterations in presynaptic release machinery that contribute to these deficits. We demonstrate that the *+/K1431M* lesion in TRIO GEF1 leads to presynaptic deficits due to Rac1 dysregulation, which can be rescued by pharmacological normalization. We propose that *Trio* variants disrupt brain function by impairing Rho GTPase signaling, causing diverse synaptic dysfunction through combined effects on pre-and/or post-synaptic functions. Our findings support growing evidence linking synaptic dysfunction in several NDD models to Rho GTPase signaling dysregulation, identifying it as a commonly affected pathway and a potential therapeutic target.

ACKNOWLEDGEMENTS

We are grateful to Xianyun Ye, Suxia Bai, Andrew Boulton, Chris Kaliszewski, and Xiao-Yuan Li for expert technical support and Bruce Herring, Katherine Roche, Dick Mains and Betty Eipper for formative discussions.

AUTHOR CONTRIBUTION

YI, ATJ and AJK designed the study and wrote the manuscript. ATJ and TN designed alleles and CRISPR strategy and AJK screened pups for germline transmission. TN and the Yale Genome Editing Center generated *Trio* CRISPR alleles. YI designed, conducted and analyzed all electrophysiology experiments. ATJ conducted dendrite reconstructions, dendritic spine analysis, measured brain and body weight, isolated crude synaptosomes and performed GLISAs. SF performed and analyzed all behavioral tests. ATJ collected samples; CMR, KN, and SAM performed and analyzed mass spectrometric measurement of proteins in brain tissue. EEC perfused animals, CAG provided support, and ATJ and YI analyzed images from electron microscopy experiments. YI identified key presynaptic and Rho GTPase targets from mass spec data. YI and ATJ conducted immunoblots and analysis. ATJ conducted Nissl stain; ATJ and MJV conducted fluorescent immunohistochemistry under YI guidance; ATJ and MJV performed IHC analysis. MGC conducted GEF assays.

CONFLICT OF INTEREST

Authors declare no conflict of interest.

FIGURE LEGENDS

Fig. 1. Genetically engineered mice with heterozygosity for K1431M, K1918X, or M2145T Trio variants have divergent effects on Trio protein expression and Rho GTPase activity.

(A) Schematic of major Trio isoforms present in the adult mouse brain, with locations of engineered neurodevelopmental disease (NDD)-associated *Trio* variants: *K1431M* is a rare missense variant in the GEF1 DH domain associated with autism spectrum disorder (ASD); a *K1918X* nonsense variant that lies just before the GEF2 domain associated with schizophrenia (SCZ); and *M2145T* missense variant in the GEF2 DH domain found in an individual with bipolar disorder (BPD). **(B)** Representative sequencing chromatograms of WT, and Trio variant mice. Arrows indicate heterozygosity for the variant alleles. **(C)** Representative immunoblots for Trio in P0 brain lysates using an antibody against Trio spectrin repeats (SR5-6). **(D)** Quantification of Trio protein levels from P0 brain lysates. Trio protein levels are reduced only in the brains of *+/K1918X* mice compared to WT controls (0.545 ± 0.126 of WT level, p=0.0046). **(E-H)** Activity levels of Rac1 (**E,G**) and RhoA (**F,H**) in whole brain homogenates of neonate (P0, **E-F**) and adult (P42, **G-H**) *Trio* variant mice as measured by G-LISA assay. Rac1 activity is increased in *+/K1431M* mice relative to WT at both ages (1.106 ± 0.027-fold at P0, p=0.0035; 1.509 ± 0.175-fold at P42, p=0.0279) and decreased in neonate *+/K1918X* mice (0.908 ± 0.0.032-fold, p=0.0230), with a trend towards increased activity in adult *+/M2145T* mice (1.438 ± 0.183-fold, p=0.0843); meanwhile RhoA activity appears unchanged in all mice relative to WT, though there may be a trend towards decreased activity in *+/K1918X* neonates (0.840 ± 0.074-fold, p=0.1292). **(I,J)** Activity levels of Rac1 (**I**) and RhoA (**J**) in synaptosomes isolated from P42 mouse cortex. Rac1 activity is increased in *+/K1431M* synaptosomes (1.125 ± 0.107-fold, p=0.0023), while RhoA activity is decreased in *+/M2145T* synaptosomes (0.731 ± 0.042-fold, p=0.0093) relative to WT. All data shown as mean ± SEM. For **(D-J)**, one-way ANOVA with post-hoc Bonferroni MC test identified differences from WT (^{ns}p<0.1, *p<0.05, **p<0.01). Mouse numbers per group are shown in bars.

Fig. 2. Heterozygosity for distinct *Trio* variants differentially impact NDD-like mouse behaviors.

(A) Schematic illustration of the behavioral tests performed on young adult (P42-P56) heterozygous *Trio* variant mice of both sexes. All mice proceeded through the same battery of tests. **(B)** *+/K1431M* and *+/K1918X* mice of both sexes had decreased latency to fall off an accelerating rotarod compared to WT male mice. In male mice (left), linear regressions identified differences from WT in slopes, indicating impaired rate of improvement in the skill (WT 16.96 ± 1.344; *+/K1431M* 7.270 ± 2.019, p<0.0001; *+/K1918X* 10.61 ± 1.444, p<0.0001; $^{\#\#\#\#}$p<0.0001) (n=40 WT; 10 *+/K1431M*; 16 *+/K1918X*; 13 *+/M2145T* male mice). In female mice (right), linear regressions identified differences from WT in slopes (*+/K1431M* 9.436 ± 2.146, p=0.0215; vs WT 14.52 ±1.792; $^{\#}$p<0.05) and intercepts (*+/K1918X* 6.492 ± 5.555, p=0.0248; vs WT 19.28 ± 5.942; $^{€}$p<0.05) (n= 28 WT; 11 *+/K1431M*; 16 13 *+/K1918X*; and 15 *+/M2145T* female mice). **(C)** *+/K1431M* mice of both sexes and *+/K1918X* females showed impaired social interactions in a three-chamber test, showing no preference to the (Str.) vs. inanimate object (Obj.) compared to WT. **(D)** *+/K1918X* mice of both sexes and *+/M2145T* females exhibit impaired novel object recognition and spend equal time exploring a novel object (N) and a familiar object (F). **(E)** Male *+/K1918X* mice exhibited increased nestlet shredding over 30 min (26.26 ± 3.61% shredded vs WT 14.26 ± 2.97%; p=0.0433), and *+/K1431M* mice exhibited a trend toward increased nestlet shredding (25.90 ± 4.34% shredded, p=0.1038) compared to WT mice. n=19 male, 19 female WT; 10 male, 10 female *+/K1431M*; 15 male, 11 female *+/K1918X*; 9 male, 10 female *+/M2145T* mice. All data are shown as mean ± SEM, significant differences identified using two-way ANOVA with post-hoc Bonferroni MC (^{ns}p<0.1, *p<0.05, **p<0.01, ***p<0.001, ****p<0.0001). Numbers of mice quantified per group are annotated inside the bar unless otherwise indicated.

Fig. 3. Trio *+/K1431M* and *+/K1918X* mice have smaller brain weights, but only +/K1918X brains have smaller less complex neurons.

(A) Ear-to-ear head width is reduced in P42 *+/K1918X* and *+/M2145T* compared to WT male mice (*+/K1431M:* 12.40 ± 0.04 mm, p=0.95; *+/K1918X:* 12.15 ± 0.08, p=0.001; *+/M2145T* 12.01 ± 0.15, p<0.0001; vs WT 12.49 ± 0.04 mm, n=17-45). **(B)** Brain weight is significantly decreased relative to WT in P42 males of all three heterozygous *Trio* variants (*+/K1431M:* 0.382 ± 0.004 g, p=0.04; *+/K1918X:* 0.346 ± 0.004 g, p<0.0001; *+/M2145T* 0.378 ± 0.005 g, p=0.002; vs WT 0.396 ± 0.004 g, n=44-98). **(C)** Body weight is significantly increased in P42 *+/K1431M* males and decreased in *+/K1918X* males (*+/K1431M:* 22.91 ± 0.38 g, p=0.01; *+/K1918X:* 20.67 ± 0.03 g, p=0.001; *+/M2145T:* 21.22 ± 0.33 g, p=0.44; vs WT 21.76 ± 0.19 g, n=45-118). **(D)** Head widths normalized to body weight of P42 *+/K1431M* male mice were reduced 10.8% compared to WT mice (*+/K1431M:* 0.520 ± 0.008 mm/g, p=0.0001; *+/K1918X:* 0.598 ± 0.012 mm/g, p>0.999; *+/M2145T* 0.607 ± 0.023 mm/g, p=0.54; vs WT 21.76 ± 0.19 mm/g, n=17-46). **(E)** Brain weights normalized to body weight of P42 *+/K1431M* and *+/K1918X* male mice were reduced 3.9% and 7.9%, respectively compared to WT mice (*+/K1431M:* 0.520 ± 0.008 mm/g, p=0.0001; *+/K1918X:* 0.598 ± 0.012 mm/g, p>0.999; *+/M2145T* 0.607 ± 0.023 mm/g, p=0.54; vs WT 21.76 ± 0.19 mm/g, n=17-46). **(F)** Representative images of Nissl-stained 30 µm coronal slices of male P42 WT and heterozygous *Trio* variant brains. **(G)** Total cross-sectional tissue area of Nissl-stained coronal sections were reduced ~9% *+/K1918X* in P42 male mice compared to WT. **(H)** Representative images of Nissl-stained cortical layers (L1-L6, dotted black box) of P42 WT and heterozygous *Trio* variant brains. **(I)** The total cortical thickness (from H) is reduced by ~8% in *+/K1918X* P42 male brains compared to WT. **(J)** Thickness of individual cortical layers, as identified in Nissl stains in Fig. 3H. L2/3 and L5 were preferentially reduced (-12% and -13%, resp.) in *+/K1918X* cortex relative to WT (L2/3: 0.306 ±0.011 mm vs WT 0.346 ±0.010 mm, p=0.0043; L5: 0.274 ±0.008 mm vs WT 0.314 ±0.008 mm, p=0.0054). **(K)** Representative traces of M1 L5 PNs from heterozygous male *Trio* variant mice crossed with *Thy1-GFP(M)*. **(L)** *+/K1918X* M1 L5 PNs show a trend toward reduced basal dendritic field size (0.1172 ± 0.0078 mm²; vs WT 0.1368 ± 0.0077 mm², p=0.0933; n=15-22 neurons per mouse), as measured by convex hull analysis of dendrite arbor reconstructions. **(M)** Both *+/K1918X* and *+/M2145T* exhibit significantly smaller apical dendritic field size *(+/K1918X*: 0.5157 ± 0.0169 mm², p=0.0460; *+/M2145T*: 0.4893 ± 0.0285 mm², p=0.0062) compared to WT (0.6081 ± 0.0319 mm²; n=15-22 neurons per mouse). All data shown as mean ± SEM. One-way ANOVA with post-hoc Bonferroni MC test identified significant differences from WT (^{ns}p<0.1, *p<0.05, **p<0.01). **(N,O)** Sholl analysis revealed basal **(N)** and apical **(O)** dendritic arborization changes in *Trio* variant M1 L5 PNs compared to WT: both basal and apical arborization was reduced in *+/K1918X*, while proximal basal arborization was increased in

+/K1431M. Two-way ANOVA (stacked) with post-hoc Bonferroni MC test identified differences from WT.

Fig. 4. *Trio* variants differentially impact synapse ultrastructure and synaptic vesicle distribution.

(A) Representative electron micrographs (EMs) from motor cortex layer 5 (M1 L5) of P42 WT and *Trio* variant mice. Post-synaptic regions are pseudo-colored in cyan; pre-synaptic regions in magenta. **(B)** Asymmetric synapse density was increased in *+/K1918X* mice (0.09205 ± 0.004775 synapses/um^2; vs WT 0.07633 ± 0.003954 synapses/um^2, p=0.0345). **(C)** PSD lengths were slightly decreased in M1 L5 synapses of by 6% in *+/K1918X* and 6.6% in *+/M2145T* mice vs WT (*+/K1918X* 0.2926 ± 0.004652 um, p=0.0204; *+/M2145T* 0.2916 ± 0.004922 um, p=0.0142; vs WT 0.3125 ± 0.005612 um). **(D,E)** Presynaptic bouton and spine head areas of *Trio* variants M1 L5 synapses were unchanged from WT. **(F)** Synaptic vesicles (SVs) distribution per 100 nm of active zone (AZ) length in M1 L5 as a function of distance from the AZ. *+/M2145T* showed an increase in readily releasable pool (RRP) identified as docked SVs (15 nm from AZ; 1.23 ± 0.05 vs WT 0.90 ± 0.05) and increase in tethered SVs (50 nm from AZ; 1.44 ± 0.04 vs WT 1.20 ± 0.05). *+/K1918X and +/M2145T* also showed an increase in the reserve pool of SVs (200 nm from AZ; 3.51 ± 0.21 and 3.81 ± 0.18, resp. vs WT 2.74 ± 0.16, n=15-30 synapses/mouse). **(G)** Total releasable pool, calculated as number of SVs at 15-150 nm from AZ per area of distribution (nm^2). RRP (15-50 nm from AZ) was significantly increased in *+/M2145T* (0.257 ± 0.007 vs WT 0.228 ± 0.008), driven by increased docked and tethered SVs. All data are presented as mean ± SEM, significance tested by ordinary one-way ANOVA with post-hoc Bonferroni MC test (*p<0.05, **p<0.01, ***p<0.001, ****p<0.0001).

Fig. 5. *Trio* variant mice exhibit deficits in synaptic signaling and LTP.

(A,D) Representative traces of miniature excitatory AMPAR-mediated mEPSCs, NMDAR-mediated mEPSCs, and **(G)** inhibitory postsynaptic currents (mIPSCs) in M1 L5 pyramidal neurons of WT and Trio variant mice. **(B)** AMPAR-mediated mEPSC amplitudes were significantly increased in *+/K1431M* (16.67 ± 1.04 pA; p=0.0009) and *+/K1918X* (14.71 ± 0.92 pA; p=0.03) slices, with no observed changes in *+/M2145T* slices (13.90 ± 1.16 pA; p=0.16) compared to WT (11.25 ± 0.84 pA; n=17-25 neurons from ≥6-8 mice per group). **(C)** No significant changes in AMPAR mEPSC frequencies (q) were observed in *+/K1431M* and *+/K1918X,* while *+/M2145T* had an increase (2.20 ± 0.15 1/s; vs WT 1.55 ± 0.09 1/s; p=0.0005). **(E, F)** NMDAR mEPSC frequencies were reduced in *+/K1431M* (0.89 ± 0.12 1/s; vs WT 1.3324 ± 0.11 1/s; p=0.015) and showed an increase in *+/M2145T* mice (1.68 ± 0.10 1/s vs WT 1.3324 ± 0.11 1/s; p=0.044, n=9-13 neurons from ≥5-7 mice per group). **(H, I)** GABA/GlyR mIPSC amplitudes were significantly increased in *+/K1918X* vs WT (23.69 ± 2.89 pA; vs 15.86 ± 1.56 pA, respectably; p=0.008), while frequency was decreased in *+/K1431M* and *+/M2145T* (0.94 ± 0.14 1/s, p<0.0001; and 1.64 ± 0.19 1/s, p=0.013; respectably; vs WT 2.44 ± 0.20; n=16-26 neurons from ≥6-8 mice per group). **(J)** Representative averaged traces of NMDA and AMPA eEPSCs recorded in M1 L5 PNs. **(K)** Heterozygous *+/K1431M* and *+/K1918X Trio* variants mice display reduced NMDAR/AMPAR eEPSC amplitude ratios, suggesting an increase in AMPAR transmission in M1 L5 PNs (*+/K1431M*: 0.75 ± 0.06, p=0.0002; *+/K1918X*: 0.69 ± 0.05, p<0.0001; *+/M2145T:* 1.00 ± 0.08, p=0.37; vs WT: 1.15 ± 0.07; n=13-19 neurons from ≥5-6 mice per group). **(L)** Averaged representative traces of baseline and post-TBS eEPSC currents in M1 L5 PNs of WT and *Trio* variant mice. **(M)** Normalized eEPSC amplitudes measuring LTP in L5 PNs by TBS in L2/3 afferents in all genotypes showed a significant decrease in the initiation and no potentiation of the LTP in *+/K1431M* and *+/K1918X*, with increase in initiation and potentiation of *+/M2145T* M1 L5 PNs compared to WT. LTP was induced at 0 min. RM two-way ANOVA with post-hoc Bonferroni MC test identified significant differences (n=6-8 neurons from ≥4-5 mice per group).

Data are presented as mean ± SEM; significance tested by one-way ANOVA with post-hoc Bonferroni test unless specified otherwise (**p<0.01; ***p<0.001; ****p<0.0001).

Fig. 6. *Trio +/K1431M and +/M2145T* variant mice have deficiencies in short-term facilitation, glutamate Pr and RRP.

(A) Representative traces in M1 L5 PNs of WT, *Trio* variant mice in response to paired pulse stimulation in L2/3. **(B)** Paired-pulse ratio (PPR) at varying interstimulus intervals (ISIs) were overlaid with a single exponential fit (except for *+/M2145T* data). An increase in the initial PPR was observed in M1 L5 PNs of *+/K1431M* slices (35 ms: 1.70 ± 0.089, p=0.003; 60 ms: 1.40 ± 0.07, p=0.046; 100 ms: 1.27 ± 0.05, p=0.031; n=20-34 neurons from ≥7-9 mice per group) with no change in *+/K1918X* slices; and in *+/M2145T* slices we observed a decrease in initial RRP at shorter ISIs (35 ms: 1.05 ± 0.06, p<0.0001; 60 ms: 0.97 ± 0.06, p=0.037) and an increase at longer ISIs (100 ms: 1.36 ± 0.09, p=0.034; 200 ms: 1.18 ± 0.08, p=0.013) compared to WT (35 ms: 1.40 ± 0.04; 60ms: 1.21 ± 0.03; 100 ms: 1.13 ± 0.03; 200 ms 1.0 ± 0.02; 300 ms 0.96 ± 0.17). **(C)** Representative traces of AMPAR eEPSCs in M1 L5 PNs under HFS (15 pulses at 40 Hz) in L2/3. **(D)** AMPAR $eEPSC_n$ amplitudes normalized to $eEPSC_1$ of the train revealed changes in the depletion rates during HFS in *Trio +/K1431M and +/M2145T* variants compared to WT (tau decay (τ_d), WT: 2.7 s, *+/K1431M:* 3.19 s, *+/M2145T:* 4.79 s, *+/K1918X:* 2.52 s; n=12-15 neurons from 5-7 mice). **(E)** The estimated glutamate probability of release (Pr) was decreased in *+/K1431M* slices (0.13 ± 0.099; p=0.013) and increased in *+/M2145T* slices (0.26 ± 0.019, p=0.042), with no significant change in *+/K1918X* slices (0.15 ±0.01, p=0.64) compared to WT M1 L5 PNs (0.19 ± 0.01; n=12-15 neurons from ≥ 5 mice per group). **(F)** The calculated size of the readily releasable vesicle pool (RRP) was increased only in *+/M2145T* M1 L5 PNs compared to WT (665.7 ± 68.5 pA vs 415.8 ± 43.9 pA, p=0.012). RRP in *+/K1431M* and *+/K1918X* synapses did not differ from WT (543.1 ± 64.4 pA; and 543.1 ± 64.4 pA, respectively vs 415.8 ± 43.9 pA) **(G)** Exponential fits of the fractional recovery plotted vs ISI, to estimate synapse ability to recover from RRP depletion. Time of recovery, measured by exponential tau recovery (τ_R), was significantly decreased in *+/K1431M* M1 L5 PNs (5.7 s, vs WT 2.2 s), *+/K1431M* also exhibited an inability to fully recover to initial levels after ISI 18 s, vs WT. Data are presented as mean ± SEM, with significant differences from WT tested using one-way ANOVA with post-hoc Bonferroni (*p<0.05; **p<0.01; ***p<0.001; ****p<0.0001).

Fig. 7 *Trio* variant mice show different molecular changes in the cortex involving presynaptic machinery and Rac1 GEFs.

(A) Bar graph illustrating the top enriched pathways (FDR q-value<0.2, *FDR<0.05) identified by gene set enrichment analysis (GSEA) for each *Trio* mutant mouse compared to WT, using all 7,362 proteins quantified by mass spectrometry in P21 cortex (n=4/genotype), sorted by normalized enrichment score (NES). Pathways with +NES are upregulated, -NES are downregulated vs. WT. [ ] indicates gene set: [R] Reactome, [WP] WikiPathways, [K] KEGG. Full list attached in Figure 7 – Source data 1 **(B,C)** Bar graphs illustrating the top enriched (FDR q-value <0.001) **(B)** cellular components and **(C)** biological processes identified by GSEA, using synaptic proteins from SynGO gene sets (n=1077 proteins), full list see in Figure 7 - Source data 2. **(D)** Representative immunoblots in synaptosomes isolated from P42 cortex of WT and *Trio* variant mice. **(E-H)** Normalized intensity levels from immunoblots demonstrate significant increases of (E) Munc18-1 (also known as syntaxin binding protein1), (F) synaptophysin (Syp), (G) syntaxin1a (Stx1) and (H) synaptotagmin3 (Syt3) levels in *+/M2145T* synaptosomes; Syp is increased while Stx1a is significantly decreased in *+/K1431M* synaptosomes compared to WT. Ordinary one-way ANOVA with post-hoc Bonferonni MC test identified differences from WT (*p<0.05, **p<0.01, ***p<0.001; n=synaptosomes from 7-14 male mice). **(I)** Representative immunoblots of select RhoGEFs from P42 cortical lysates of WT and *Trio* variant mice. **(J-L)** Normalized intensity levels from immunoblots identified ~47% increase of Tiam1 levels in *+/K1431M* and increase ~45% in *+/M2145T* cortex vs to WT; VAV2 is increased ~34% in *+/M2145T* cortex compared to WT. Unpaired t-tests identified differences from WT (*p<0.05; n=6 mice per genotype).

Figure 7 – Source data 1. Gene Set Enrichment Analysis of P21 cortex proteome of *Trio* WT, *+/K1431M*, *+/K1918X*, and *+/M2145T* mice.

Figure 7 - Source data 2. Synaptic Gene Ontologies (SynGO) of P21 cortex proteome of *Trio* WT, *+/K1431M*, *+/K1918X*, and *+/M2145T* mice.

Fig. 8. NSC, Rac1 inhibitor application rescued Pr in *+/K1431M* L23-L5 synapses and improves SV recycling.

(A) Representative PPR traces of WT and *Trio +/K1431M* slices with or without 5 min application of 100 µM NSC23766. **(B)** Acute application of NSC onto both *+/K1431M* and WT synapses lead to decrease in PPF in M1 L2/3-L5 synapses. *+/K1431*M slices significantly shifted the PPF curve at all ISI downwards compared to untreated *+/K1431M* slices, and showed no significant difference from WT (*+/K1431M* +NSC 35 ms: 1.25 ± 0.06, p<0.0001; 60 ms: 1.13 ± 0.052, p=0.0007; 100 ms: 1.02 ± 0.053, p=0.0017; 200 ms 0.91 ± 0.039, p=0.0043; 300 ms 0.88 ± 0.045, p=0.021), with *+/K1431M* shifting into paired pulse depression at 200-300 ms intervals, while WT PPF plateauing to 1. **(C)** Representative traces of AMPAR eEPSCs in M1 L5 PNs under HFS of WT and *Trio +/K1431M* slices before and after NSC application. **(D)** Normalized AMPAR $eEPSC_n$ amplitudes of the train revealed changes in the depletion rates during HFS before and after NSC application to WT and *+/K1431M* slices (tau decay (τ_d), WT+NSC: 2.85 s vs WT: 2.70 s; *+/K1431M*+NSC*:* 2.66 s vs *+/K1431M:* 3.19 s, n=12-15 neurons from 5-7 mice). **(E)** Rac1 inhibition by NSC increased the glutamate Pr in both WT and *+/K1431M* slices (WT + NSC 0.25 ± 0.067 vs initial 0.19 ± 0.01, p=0.046; and for *+/K1431M* + NSC 0.23 ± 0.019 vs initial 0.13 ± 0.099, p<0.0001; n=15-18 neurons from ≥ 5 mice per group). **(F)** RRP in WT or *+/K1431M* synapses with NSC did not show significant changes to initial values (WT +NSC: 370.3 ± 82.37 pA vs 415.8 ± 43.9 pA, p□0.99; *+/K1431M* + NSC: 427.9 ± 79.2 vs 543.1 ± 64.44 pA, p□0.99). **(G)** Exponential fits of the fractional recovery for WT and *+/K1431M* with and without NSC application. NSC application led to a faster recovery time in WT (+NSC: 1.5 s vs initial 2.2 s) and it significantly improved but did not fully rescue recovery time in *+/K1431M* (+ NSC 3.2 s vs initial 5.7 s), but allowed for full recovery at 18s. Data are presented as mean ± SEM, significance tested using one-way ANOVA with post-hoc Bonferroni (*p<0.05; **p<0.01; ***p<0.001; ****p<0.0001).

REFERENCES

1. American Psychiatric Association. Diagnostic and Statistical Manual of Mental Disorders. 5th ed. Washington, DC2013.
2. Anttila V, Bulik-Sullivan B, Finucane HK, Walters RK, Bras J, Duncan L, et al. Analysis of shared heritability in common disorders of the brain. Science. 2018;360(6395):1313-+.
3. Debant A, Serra-Pages C, Seipel K, O'Brien S, Tang M, Park SH, et al. The multidomain protein Trio binds the LAR transmembrane tyrosine phosphatase, contains a protein kinase domain, and has separate rac-specific and rho-specific guanine nucleotide exchange factor domains. Proc Natl Acad Sci U S A. 1996;93(11):5466-71.
4. Bellanger JM, Lazaro JB, Diriong S, Fernandez A, Lamb N, Debant A. The two guanine nucleotide exchange factor domains of Trio link the Rac1 and the RhoA pathways in vivo. Oncogene. 1998;16(2):147-52.
5. Blangy A, Vignal E, Schmidt S, Debant A, Gauthier-Rouviere C, Fort P. TrioGEF1 controls Rac- and Cdc42-dependent cell structures through the direct activation of rhoG. J Cell Sci. 2000;113 (Pt 4):729-39.
6. Grubisha MJ, DeGiosio RA, Wills ZP, Sweet RA. Trio and Kalirin as unique enactors of Rho/Rac spatiotemporal precision. Cell Signal. 2022;98:110416.
7. Paskus JD, Herring BE, Roche KW. Kalirin and Trio: RhoGEFs in Synaptic Transmission, Plasticity, and Complex Brain Disorders. Trends Neurosci. 2020;43(7):505-18.
8. Duman JG, Mulherkar S, Tu YK, J XC, Tolias KF. Mechanisms for spatiotemporal regulation of Rho-GTPase signaling at synapses. Neurosci Lett. 2015;601:4-10.
9. Hall A. Rho GTPases and the actin cytoskeleton. Science. 1998;279(5350):509-14.
10. Luo L. Rho GTPases in neuronal morphogenesis. Nat Rev Neurosci. 2000;1(3):173-80.
11. Nakayama AY, Harms MB, Luo L. Small GTPases Rac and Rho in the maintenance of dendritic spines and branches in hippocampal pyramidal neurons. J Neurosci. 2000;20(14):5329-38.
12. Newey SE, Velamoor V, Govek EE, Van Aelst L. Rho GTPases, dendritic structure, and mental retardation. J Neurobiol. 2005;64(1):58-74.
13. Terry-Lorenzo RT, Torres VI, Wagh D, Galaz J, Swanson SK, Florens L, et al. Trio, a Rho Family GEF, Interacts with the Presynaptic Active Zone Proteins Piccolo and Bassoon. PLoS One. 2016;11(12):e0167535.
14. O'Neil SD, Racz B, Brown WE, Gao Y, Soderblom EJ, Yasuda R, et al. Action potential-coupled Rho GTPase signaling drives presynaptic plasticity. Elife. 2021;10.
15. O'Brien SP, Seipel K, Medley QG, Bronson R, Segal R, Streuli M. Skeletal muscle deformity and neuronal disorder in Trio exchange factor-deficient mouse embryos. Proc Natl Acad Sci U S A. 2000;97(22):12074-8.
16. Peng YJ, He WQ, Tang J, Tao T, Chen C, Gao YQ, et al. Trio is a key guanine nucleotide exchange factor coordinating regulation of the migration and morphogenesis of granule cells in the developing cerebellum. J Biol Chem. 2010;285(32):24834-44.
17. Zong W, Liu S, Wang X, Zhang J, Zhang T, Liu Z, et al. Trio gene is required for mouse learning ability. Brain Res. 2015;1608:82-90.
18. Katrancha SM, Shaw JE, Zhao AY, Myers SA, Cocco AR, Jeng AT, et al. Trio Haploinsufficiency Causes Neurodevelopmental Disease-Associated Deficits. Cell Rep. 2019;26(10):2805-17 e9.
19. Sun X, Wang L, Wei C, Sun M, Li Q, Meng H, et al. Dysfunction of Trio GEF1 involves in excitatory/inhibitory imbalance and autism-like behaviors through regulation of interneuron migration. Mol Psychiatry. 2021.
20. Tian C, Paskus JD, Fingleton E, Roche KW, Herring BE. Autism Spectrum Disorder/Intellectual Disability-associated mutations in Trio disrupt Neuroligin 1-mediated synaptogenesis. J Neurosci. 2021.

21. Paskus JD, Tian C, Fingleton E, Shen C, Chen X, Li Y, et al. Synaptic Kalirin-7 and Trio Interactomes Reveal a GEF Protein-Dependent Neuroligin-1 Mechanism of Action. Cell Rep. 2019;29(10):2944-52 e5.
22. Ba W, Yan Y, Reijnders MR, Schuurs-Hoeijmakers JH, Feenstra I, Bongers EM, et al. TRIO loss of function is associated with mild intellectual disability and affects dendritic branching and synapse function. Hum Mol Genet. 2016;25(5):892-902.
23. Katrancha SM, Wu Y, Zhu M, Eipper BA, Koleske AJ, Mains RE. Neurodevelopmental disease-associated de novo mutations and rare sequence variants affect TRIO GDP/GTP exchange factor activity. Hum Mol Genet. 2017.
24. Barbosa S, Greville-Heygate S, Bonnet M, Godwin A, Fagotto-Kaufmann C, Kajava AV, et al. Opposite Modulation of RAC1 by Mutations in TRIO Is Associated with Distinct, Domain-Specific Neurodevelopmental Disorders. Am J Hum Genet. 2020;106(3):338-55.
25. Bonnet M, Roche F, Fagotto-Kaufmann C, Gazdagh G, Truong I, Comunale F, et al. Pathogenic TRIO variants associated with neurodevelopmental disorders perturb the molecular regulation of TRIO and axon pathfinding in vivo. Mol Psychiatry. 2023;28(4):1527-44.
26. Gazdagh G, Hunt D, Gonzalez AMC, Rodriguez MP, Chaudhry A, Madruga M, et al. Extending the phenotypes associated with TRIO gene variants in a cohort of 25 patients and review of the literature. Am J Med Genet A. 2023;191(7):1722-40.
27. Pengelly RJ, Greville-Heygate S, Schmidt S, Seaby EG, Jabalameli MR, Mehta SG, et al. Mutations specific to the Rac-GEF domain of TRIO cause intellectual disability and microcephaly. J Med Genet. 2016;53(11):735-42.
28. Sadybekov A, Tian C, Arnesano C, Katritch V, Herring BE. An autism spectrum disorder-related de novo mutation hotspot discovered in the GEF1 domain of Trio. Nat Commun. 2017;8(1):601.
29. Singh T, Poterba T, Curtis D, Akil H, Al Eissa M, Barchas JD, et al. Rare coding variants in ten genes confer substantial risk for schizophrenia. Nature. 2022;604(7906):509-16.
30. Howrigan DP, Rose SA, Samocha KE, Fromer M, Cerrato F, Chen WJ, et al. Exome sequencing in schizophrenia-affected parent-offspring trios reveals risk conferred by protein-coding de novo mutations. Nat Neurosci. 2020;23(2):185-93.
31. Kloth K, Graul-Neumann L, Hermann K, Johannsen J, Bierhals T, Kortum F. More evidence on TRIO missense mutations in the spectrin repeat domain causing severe developmental delay and recognizable facial dysmorphism with macrocephaly. Neurogenetics. 2021;22(3):221-4.
32. Bircher JE, Corcoran EE, Lam TT, Trnka MJ, Koleske AJ. Autoinhibition of the GEF activity of cytoskeletal regulatory protein Trio is disrupted in neurodevelopmental disorder-related genetic variants. The Journal of biological chemistry. 2022;298(9):102361.
33. Barbosa S, Greville-Heygate S, Bonnet M, Godwin A, Fagotto-Kaufmann C, Kajava AV, et al. Opposite Modulation of RAC1 by Mutations in TRIO Is Associated with Distinct, Domain-Specific Neurodevelopmental Disorders. Am J Hum Genet. 2020;106(3):338-55.
34. Bonnet M, Roche F, Fagotto-Kaufmann C, Gazdagh G, Truong I, Comunale F, et al. Pathogenic TRIO variants associated with neurodevelopmental disorders perturb the molecular regulation of TRIO and axon pathfinding in vivo. Mol Psychiatry. 2023;28(4):1527-44.
35. Frankfurt M, Luine V. The evolving role of dendritic spines and memory: Interaction(s) with estradiol. Horm Behav. 2015;74:28-36.
36. Yang H, Wang H, Jaenisch R. Generating genetically modified mice using CRISPR/Cas-mediated genome engineering. Nat Protoc. 2014;9(8):1956-68.
37. Chen S, Lee B, Lee AY, Modzelewski AJ, He L. Highly Efficient Mouse Genome Editing by CRISPR Ribonucleoprotein Electroporation of Zygotes. The Journal of biological chemistry. 2016;291(28):14457-67.
38. Haeussler M, Schonig K, Eckert H, Eschstruth A, Mianne J, Renaud JB, et al. Evaluation of off-target and on-target scoring algorithms and integration into the guide RNA selection tool CRISPOR. Genome Biol. 2016;17(1):148.

39. Nagy A. Manipulating the mouse embryo : a laboratory manual. 3rd ed. Cold Spring Harbor, N.Y.: Cold Spring Harbor Laboratory Press; 2003. x, 764 p. p.
40. Blaise AM, Corcoran EE, Wattenberg ES, Zhang YL, Cottrell JR, Koleske AJ. In vitro fluorescence assay to measure GDP/GTP exchange of guanine nucleotide exchange factors of Rho family GTPases. Biol Methods Protoc. 2022;7(1):bpab024.
41. Hollingsworth EB, McNeal ET, Burton JL, Williams RJ, Daly JW, Creveling CR. Biochemical characterization of a filtered synaptoneurosome preparation from guinea pig cerebral cortex: cyclic adenosine 3':5'-monophosphate-generating systems, receptors, and enzymes. J Neurosci. 1985;5(8):2240-53.
42. Scheetz AJ, Nairn AC, Constantine-Paton M. NMDA receptor-mediated control of protein synthesis at developing synapses. Nat Neurosci. 2000;3(3):211-6.
43. Deacon RM. Measuring the strength of mice. J Vis Exp. 2013(76).
44. Omar MH, Kerrisk Campbell M, Xiao X, Zhong Q, Brunken WJ, Miner JH, et al. CNS Neurons Deposit Laminin alpha5 to Stabilize Synapses. Cell Rep. 2017;21(5):1281-92.
45. Rapanelli M, Frick LR, Xu M, Groman SM, Jindachomthong K, Tamamaki N, et al. Targeted Interneuron Depletion in the Dorsal Striatum Produces Autism-like Behavioral Abnormalities in Male but Not Female Mice. Biol Psychiatry. 2017;82(3):194-203.
46. Sfakianos MK, Eisman A, Gourley SL, Bradley WD, Scheetz AJ, Settleman J, et al. Inhibition of Rho via Arg and p190RhoGAP in the postnatal mouse hippocampus regulates dendritic spine maturation, synapse and dendrite stability, and behavior. J Neurosci. 2007;27(41):10982-92.
47. Paul CA, Beltz B, Berger-Sweeney J. The nissl stain: a stain for cell bodies in brain sections. CSH Protoc. 2008;2008:pdb prot4805.
48. Franklin KBJ, Paxinos G. Paxinos and Franklin's The mouse brain in stereotaxic coordinates. Fourth edition. ed. Amsterdam: Academic Press, an imprint of Elsevier; 2013. 1 volume (unpaged) p.
49. Feng G, Mellor RH, Bernstein M, Keller-Peck C, Nguyen QT, Wallace M, et al. Imaging neuronal subsets in transgenic mice expressing multiple spectral variants of GFP. Neuron. 2000;28(1):41-51.
50. Levy AD, Xiao X, Shaw JE, Sudarsana Devi SP, Katrancha SM, Bennett AM, et al. Noonan Syndrome-Associated SHP2 Dephosphorylates GluN2B to Regulate NMDA Receptor Function. Cell Rep. 2018;24(6):1523-35.
51. Gonzalez-Forero D, Montero F, Garcia-Morales V, Dominguez G, Gomez-Perez L, Garcia-Verdugo JM, et al. Endogenous Rho-kinase signaling maintains synaptic strength by stabilizing the size of the readily releasable pool of synaptic vesicles. J Neurosci. 2012;32(1):68-84.
52. Montesinos MS, Dong W, Goff K, Das B, Guerrero-Given D, Schmalzigaug R, et al. Presynaptic Deletion of GIT Proteins Results in Increased Synaptic Strength at a Mammalian Central Synapse. Neuron. 2015;88(5):918-25.
53. Dong W, Radulovic T, Goral RO, Thomas C, Suarez Montesinos M, Guerrero-Given D, et al. CAST/ELKS Proteins Control Voltage-Gated Ca(2+) Channel Density and Synaptic Release Probability at a Mammalian Central Synapse. Cell Rep. 2018;24(2):284-93 e6.
54. Ruiz R, Cano R, Casanas JJ, Gaffield MA, Betz WJ, Tabares L. Active zones and the readily releasable pool of synaptic vesicles at the neuromuscular junction of the mouse. J Neurosci. 2011;31(6):2000-8.
55. Thanawala MS, Regehr WG. Determining synaptic parameters using high-frequency activation. J Neurosci Methods. 2016;264:136-52.
56. Mertins P, Tang LC, Krug K, Clark DJ, Gritsenko MA, Chen L, et al. Reproducible workflow for multiplexed deep-scale proteome and phosphoproteome analysis of tumor tissues by liquid chromatography-mass spectrometry. Nat Protoc. 2018;13(7):1632-61.
57. Subramanian A, Tamayo P, Mootha VK, Mukherjee S, Ebert BL, Gillette MA, et al. Gene set enrichment analysis: a knowledge-based approach for interpreting genome-wide expression profiles. Proc Natl Acad Sci U S A. 2005;102(43):15545-50.

58. Mootha VK, Lindgren CM, Eriksson KF, Subramanian A, Sihag S, Lehar J, et al. PGC-1alpha-responsive genes involved in oxidative phosphorylation are coordinately downregulated in human diabetes. Nat Genet. 2003;34(3):267-73.
59. Koopmans F, van Nierop P, Andres-Alonso M, Byrnes A, Cijsouw T, Coba MP, et al. SynGO: An Evidence-Based, Expert-Curated Knowledge Base for the Synapse. Neuron. 2019;103(2):217-34 e4.
60. Bircher JE, Koleske AJ. Trio family proteins as regulators of cell migration and morphogenesis in development and disease - mechanisms and cellular contexts. J Cell Sci. 2021;134(3).
61. McPherson CE, Eipper BA, Mains RE. Multiple novel isoforms of Trio are expressed in the developing rat brain. Gene. 2005;347(1):125-35.
62. Portales-Casamar E, Briancon-Marjollet A, Fromont S, Triboulet R, Debant A. Identification of novel neuronal isoforms of the Rho-GEF Trio. Biol Cell. 2006;98(3):183-93.
63. Oevel K, Hohensee S, Kumar A, Rosas-Brugada I, Bartolini F, Soykan T, et al. Rho GTPase signaling and mDia facilitate endocytosis via presynaptic actin. Elife. 2024;12.
64. Ridley RM. The Psychology of Perseverative and Stereotyped Behavior. Progress in Neurobiology. 1994;44(2):221-31.
65. Wei C, Sun M, Sun X, Meng H, Li Q, Gao K, et al. RhoGEF Trio Regulates Radial Migration of Projection Neurons via Its Distinct Domains. Neurosci Bull. 2022;38(3):249-62.
66. Kaufmann WE, Moser HW. Dendritic anomalies in disorders associated with mental retardation. Cereb Cortex. 2000;10(10):981-91.
67. Huttenlocher PR. Dendritic development and mental defect. Neurology. 1970;20(4):381.
68. Huttenlocher PR. Dendritic development in neocortex of children with mental defect and infantile spasms. Neurology. 1974;24(3):203-10.
69. Huttenlocher PR. Dendritic and synaptic pathology in mental retardation. Pediatr Neurol. 1991;7(2):79-85.
70. Purpura DP. Dendritic spine "dysgenesis" and mental retardation. Science. 1974;186(4169):1126-8.
71. Purpura DP. Dendritic differentiation in human cerebral cortex: normal and aberrant developmental patterns. Adv Neurol. 1975;12:91-134.
72. Kulkarni VA, Firestein BL. The dendritic tree and brain disorders. Mol Cell Neurosci. 2012;50(1):10-20.
73. Yan Y, Eipper BA, Mains RE. Kalirin-9 and Kalirin-12 Play Essential Roles in Dendritic Outgrowth and Branching. Cereb Cortex. 2015;25(10):3487-501.
74. Keine C, Al-Yaari M, Radulovic T, Thomas CI, Valino Ramos P, Guerrero-Given D, et al. Presynaptic Rac1 controls synaptic strength through the regulation of synaptic vesicle priming. Elife. 2022;11.
75. Carroll LS, Owen MJ. Genetic overlap between autism, schizophrenia and bipolar disorder. Genome Med. 2009;1(10):102.
76. Purcell SM, Moran JL, Fromer M, Ruderfer D, Solovieff N, Roussos P, et al. A polygenic burden of rare disruptive mutations in schizophrenia. Nature. 2014;506(7487):185-90.
77. Satterstrom FK, Kosmicki JA, Wang JB, Breen MS, De Rubeis S, An JY, et al. Large-Scale Exome Sequencing Study Implicates Both Developmental and Functional Changes in the Neurobiology of Autism. Cell. 2020;180(3):568-+.
78. Genovese G, Fromer M, Stahl EA, Ruderfer DM, Chambert K, Landen M, et al. Increased burden of ultra-rare protein-altering variants among 4,877 individuals with schizophrenia. Nat Neurosci. 2016;19(11):1433-41.
79. Fromer M, Pocklington AJ, Kavanagh DH, Williams HJ, Dwyer S, Gormley P, et al. De novo mutations in schizophrenia implicate synaptic networks. Nature. 2014;506(7487):179-84.
80. De Rubeis S, He X, Goldberg AP, Poultney CS, Samocha K, Cicek AE, et al. Synaptic, transcriptional and chromatin genes disrupted in autism. Nature. 2014;515(7526):209-15.

81. Iossifov I, O'Roak BJ, Sanders SJ, Ronemus M, Krumm N, Levy D, et al. The contribution of de novo coding mutations to autism spectrum disorder. Nature. 2014;515(7526):216-21.
82. Pinto D, Delaby E, Merico D, Barbosa M, Merikangas A, Klei L, et al. Convergence of genes and cellular pathways dysregulated in autism spectrum disorders. Am J Hum Genet. 2014;94(5):677-94.
83. Kirov G, Pocklington AJ, Holmans P, Ivanov D, Ikeda M, Ruderfer D, et al. De novo CNV analysis implicates specific abnormalities of postsynaptic signalling complexes in the pathogenesis of schizophrenia. Mol Psychiatry. 2012;17(2):142-53.
84. Schultz-Rogers L, Muthusamy K, Pinto EVF, Klee EW, Lanpher B. Novel loss-of-function variants in TRIO are associated with neurodevelopmental disorder: case report. BMC Med Genet. 2020;21(1):219.
85. Bolte S, Neufeld J, Marschik PB, Williams ZJ, Gallagher L, Lai MC. Sex and gender in neurodevelopmental conditions. Nat Rev Neurol. 2023;19(3):136-59.
86. Howes OD, Cummings C, Chapman GE, Shatalina E. Neuroimaging in schizophrenia: an overview of findings and their implications for synaptic changes. Neuropsychopharmacology. 2023;48(1):151-67.
87. Dabiri M, Dehghani Firouzabadi F, Yang K, Barker PB, Lee RR, Yousem DM. Neuroimaging in schizophrenia: A review article. Front Neurosci. 2022;16:1042814.
88. Harvey I, Ron MA, Du Boulay G, Wicks D, Lewis SW, Murray RM. Reduction of cortical volume in schizophrenia on magnetic resonance imaging. Psychol Med. 1993;23(3):591-604.
89. Suddath RL, Casanova MF, Goldberg TE, Daniel DG, Kelsoe JR, Jr., Weinberger DR. Temporal lobe pathology in schizophrenia: a quantitative magnetic resonance imaging study. Am J Psychiatry. 1989;146(4):464-72.
90. Zipursky RB, Lim KO, Sullivan EV, Brown BW, Pfefferbaum A. Widespread cerebral gray matter volume deficits in schizophrenia. Arch Gen Psychiatry. 1992;49(3):195-205.
91. Kowluru A. Friendly, and not so friendly, roles of Rac1 in islet beta-cell function: lessons learnt from pharmacological and molecular biological approaches. Biochem Pharmacol. 2011;81(8):965-75.
92. Kowluru A. Multiple Guanine Nucleotide Exchange Factors Mediate Glucose-Induced Rac1 Activation and Insulin Secretion: Is It Precise Regulatory Control or a Case of Two Peas from the Same Pod? ACS Pharmacol Transl Sci. 2021;4(5):1702-4.
93. Zhou S, Yu D, Ning S, Zhang H, Jiang L, He L, et al. Augmented Rac1 Expression and Activity are Associated with Oxidative Stress and Decline of beta Cell Function in Obesity. Cell Physiol Biochem. 2015;35(6):2135-48.
94. Veluthakal R, Thurmond DC. Emerging Roles of Small GTPases in Islet beta-Cell Function. Cells. 2021;10(6).
95. Asahara S, Shibutani Y, Teruyama K, Inoue HY, Kawada Y, Etoh H, et al. Ras-related C3 botulinum toxin substrate 1 (RAC1) regulates glucose-stimulated insulin secretion via modulation of F-actin. Diabetologia. 2013;56(5):1088-97.
96. Sylow L, Nielsen IL, Kleinert M, Moller LL, Ploug T, Schjerling P, et al. Rac1 governs exercise-stimulated glucose uptake in skeletal muscle through regulation of GLUT4 translocation in mice. J Physiol. 2016;594(17):4997-5008.
97. Ba W, van der Raadt J, Nadif Kasri N. Rho GTPase signaling at the synapse: implications for intellectual disability. Exp Cell Res. 2013;319(15):2368-74.
98. Broadbelt K, Byne W, Jones LB. Evidence for a decrease in basilar dendrites of pyramidal cells in schizophrenic medial prefrontal cortex. Schizophr Res. 2002;58(1):75-81.
99. Black JE, Kodish IM, Grossman AW, Klintsova AY, Orlovskaya D, Vostrikov V, et al. Pathology of layer V pyramidal neurons in the prefrontal cortex of patients with schizophrenia. Am J Psychiatry. 2004;161(4):742-4.
100. Ramaswamy S, Markram H. Anatomy and physiology of the thick-tufted layer 5 pyramidal neuron. Front Cell Neurosci. 2015;9:233.

101. Chen L, Melendez J, Campbell K, Kuan CY, Zheng Y. Rac1 deficiency in the forebrain results in neural progenitor reduction and microcephaly. Dev Biol. 2009;325(1):162-70.
102. Reijnders MRF, Ansor NM, Kousi M, Yue WW, Tan PL, Clarkson K, et al. RAC1 Missense Mutations in Developmental Disorders with Diverse Phenotypes. Am J Hum Genet. 2017;101(3):466-77.
103. Tahirovic S, Hellal F, Neukirchen D, Hindges R, Garvalov BK, Flynn KC, et al. Rac1 regulates neuronal polarization through the WAVE complex. J Neurosci. 2010;30(20):6930-43.
104. Pennucci R, Gucciardi I, de Curtis I. Rac1 and Rac3 GTPases differently influence the morphological maturation of dendritic spines in hippocampal neurons. PLoS One. 2019;14(8):e0220496.
105. Wiens KM, Lin H, Liao D. Rac1 induces the clustering of AMPA receptors during spinogenesis. J Neurosci. 2005;25(46):10627-36.
106. Ba W, Nadif Kasri N. RhoGTPases at the synapse: An embarrassment of choice. Small GTPases. 2017;8(2):106-13.
107. Pertz O. Spatio-temporal Rho GTPase signaling - where are we now? J Cell Sci. 2010;123(Pt 11):1841-50.
108. Bellanger JM, Astier C, Sardet C, Ohta Y, Stossel TP, Debant A. The Rac1- and RhoG-specific GEF domain of Trio targets filamin to remodel cytoskeletal actin. Nat Cell Biol. 2000;2(12):888-92.
109. Scala M, Nishikawa M, Nagata KI, Striano P. Pathophysiological Mechanisms in Neurodevelopmental Disorders Caused by Rac GTPases Dysregulation: What's behind Neuro-RACopathies. Cells. 2021;10(12).
110. Hajdo-Milasinovic A, Ellenbroek SI, van Es S, van der Vaart B, Collard JG. Rac1 and Rac3 have opposing functions in cell adhesion and differentiation of neuronal cells. J Cell Sci. 2007;120(Pt 4):555-66.
111. Corbetta S, Gualdoni S, Ciceri G, Monari M, Zuccaro E, Tybulewicz VL, et al. Essential role of Rac1 and Rac3 GTPases in neuronal development. FASEB J. 2009;23(5):1347-57.
112. Pinto D, Pagnamenta AT, Klei L, Anney R, Merico D, Regan R, et al. Functional impact of global rare copy number variation in autism spectrum disorders. Nature. 2010;466(7304):368-72.
113. Zeidan-Chulia F, Rybarczyk-Filho JL, Salmina AB, de Oliveira BH, Noda M, Moreira JC. Exploring the multifactorial nature of autism through computational systems biology: calcium and the Rho GTPase RAC1 under the spotlight. Neuromolecular Med. 2013;15(2):364-83.
114. Guo D, Yang X, Shi L. Rho GTPase Regulators and Effectors in Autism Spectrum Disorders: Animal Models and Insights for Therapeutics. Cells. 2020;9(4).
115. Carbonell AU, Freire-Cobo C, Deyneko IV, Dobariya S, Erdjument-Bromage H, Clipperton-Allen AE, et al. Comparing synaptic proteomes across five mouse models for autism reveals converging molecular similarities including deficits in oxidative phosphorylation and Rho GTPase signaling. Front Aging Neurosci. 2023;15:1152562.
116. Zamboni V, Armentano M, Berto G, Ciraolo E, Ghigo A, Garzotto D, et al. Hyperactivity of Rac1-GTPase pathway impairs neuritogenesis of cortical neurons by altering actin dynamics. Sci Rep. 2018;8(1):7254.
117. Hussain NK, Thomas GM, Luo J, Huganir RL. Regulation of AMPA receptor subunit GluA1 surface expression by PAK3 phosphorylation. Proceedings of the National Academy of Sciences. 2015;112(43):E5883-E90.
118. Cui D, Jiang X, Chen M, Sheng H, Shao D, Yang L, et al. Activation of Rac1 Has an Opposing Effect on Induction and Maintenance of Long-Term Potentiation in Hippocampus by Acting on Different Kinases. Front Mol Neurosci. 2021;14:720371.
119. Herring BE, Nicoll RA. Long-Term Potentiation: From CaMKII to AMPA Receptor Trafficking. Annu Rev Physiol. 2016;78:351-65.

120. Duman JG, Blanco FA, Cronkite CA, Ru Q, Erikson KC, Mulherkar S, et al. Rac-maninoff and Rho-vel: The symphony of Rho-GTPase signaling at excitatory synapses. Small GTPases. 2022;13(1):14-47.
121. Ferraro F, Ma XM, Sobota JA, Eipper BA, Mains RE. Kalirin/Trio Rho guanine nucleotide exchange factors regulate a novel step in secretory granule maturation. Mol Biol Cell. 2007;18(12):4813-25.
122. Hong-Geller E, Cerione RA. Cdc42 and Rac stimulate exocytosis of secretory granules by activating the IP(3)/calcium pathway in RBL-2H3 mast cells. J Cell Biol. 2000;148(3):481-94.
123. Lecuona E, Ridge K, Pesce L, Batlle D, Sznajder JI. The GTP-binding protein RhoA mediates Na,K-ATPase exocytosis in alveolar epithelial cells. Mol Biol Cell. 2003;14(9):3888-97.
124. Momboisse F, Lonchamp E, Calco V, Ceridono M, Vitale N, Bader MF, et al. betaPIX-activated Rac1 stimulates the activation of phospholipase D, which is associated with exocytosis in neuroendocrine cells. J Cell Sci. 2009;122(Pt 6):798-806.
125. Pathak R, Delorme-Walker VD, Howell MC, Anselmo AN, White MA, Bokoch GM, et al. The microtubule-associated Rho activating factor GEF-H1 interacts with exocyst complex to regulate vesicle traffic. Dev Cell. 2012;23(2):397-411.
126. Doussau F, Gasman S, Humeau Y, Vitiello F, Popoff M, Boquet P, et al. A Rho-related GTPase is involved in Ca(2+)-dependent neurotransmitter exocytosis. The Journal of biological chemistry. 2000;275(11):7764-70.
127. Banerjee S, Vernon S, Ruchti E, Limoni G, Jiao W, Asadzadeh J, et al. Trio preserves motor synapses and prolongs motor ability during aging. Cell Rep. 2024;43(6):114256.
128. Weingarten DJ, Shrestha A, Juda-Nelson K, Kissiwaa SA, Spruston E, Jackman SL. Fast resupply of synaptic vesicles requires synaptotagmin-3. Nature. 2022;611(7935):320-5.

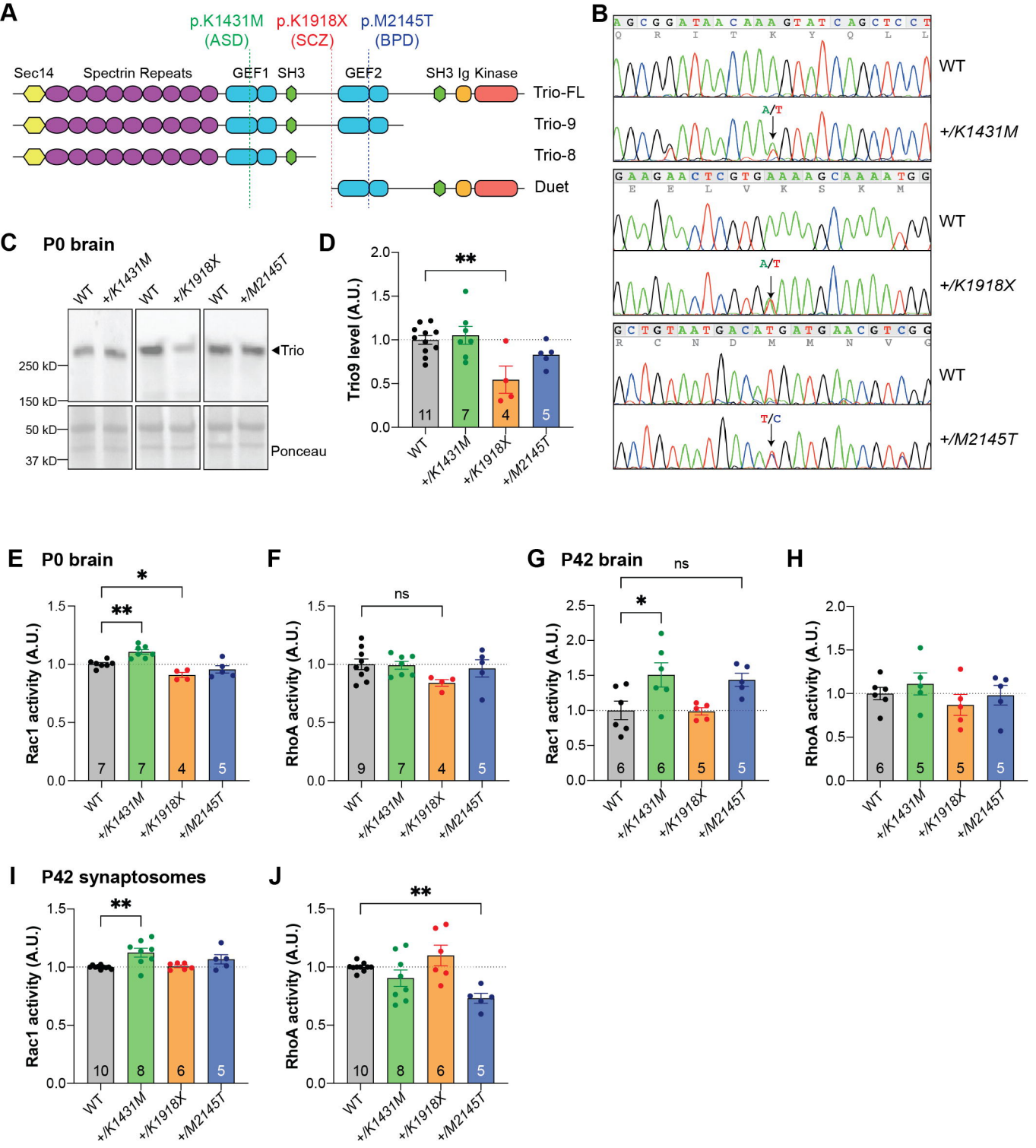
A
p.K1431M (ASD)
p.K1918X (SCZ)
p.M2145T (BPD)
Sec14
Spectrin Repeats
GEF1
SH3
GEF2
SH3 Ig Kinase
Trio-FL
Trio-9
Trio-8
Duet
B
WT
+/K1431M
+/K1918X
+/M2145T
A/T
T/C
C
P0 brain
WT
+/K1431M
+/K1918X
+/M2145T
Trio
250 kD
150 kD
50 kD
37 kD
Ponceau
D
Trio9 level (A.U.)
E
P0 brain
Rac1 activity (A.U.)
F
RhoA activity (A.U.)
G
P42 brain
Rac1 activity (A.U.)
H
RhoA activity (A.U.)
I
P42 synaptosomes
Rac1 activity (A.U.)
J
RhoA activity (A.U.)
ns

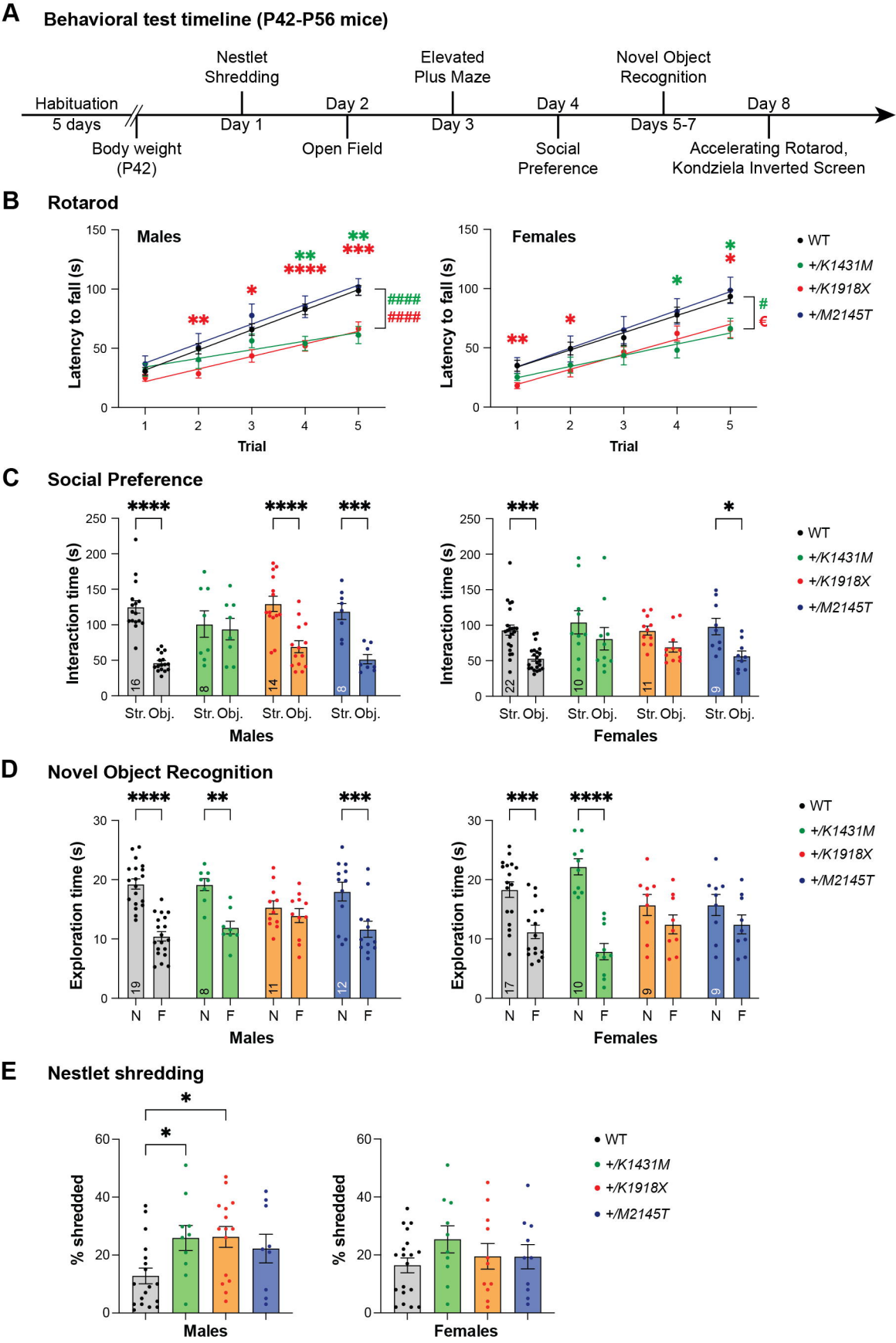
A
Behavioral test timeline (P42-P56 mice)
Habituation
5 days
Body weight
(P42)
Nestlet
Shredding
Day 1
Day 2
Open Field
Elevated
Plus Maze
Day 3
Day 4
Social
Preference
Novel Object
Recognition
Days 5-7
Day 8
Accelerating Rotarod,
Kondziela Inverted Screen
B
Rotarod
Males
Females
Latency to fall (s)
Trial
WT
+/K1431M
+/K1918X
+/M2145T
C
Social Preference
Interaction time (s)
Str.
Obj.
Males
Females
D
Novel Object Recognition
Exploration time (s)
N
F
E
Nestlet shredding
% shredded

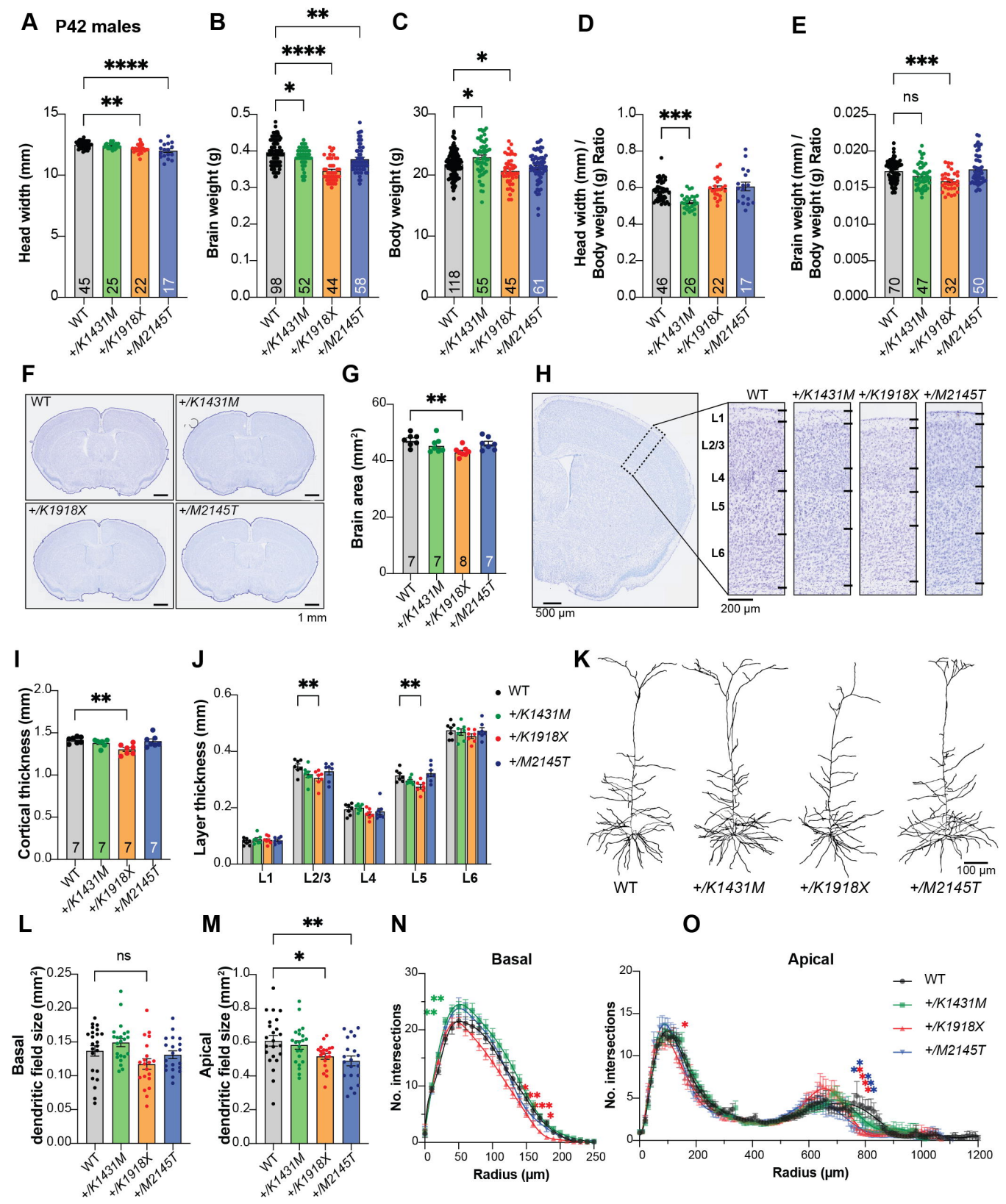
A
P42 males
Head width (mm)
B
Brain weight (g)
C
Body weight (g)
D
Head width (mm) / Body weight (g) Ratio
E
Brain weight (mm) / Body weight (g) Ratio
ns
WT
+/K1431M
+/K1918X
+/M2145T
F
1 mm
G
Brain area (mm²)
H
500 µm
200 µm
L1
L2/3
L4
L5
L6
I
Cortical thickness (mm)
J
Layer thickness (mm)
K
100 µm
L
Basal dendritic field size (mm²)
M
Apical dendritic field size (mm²)
N
Basal
No. intersections
Radius (µm)
O
Apical

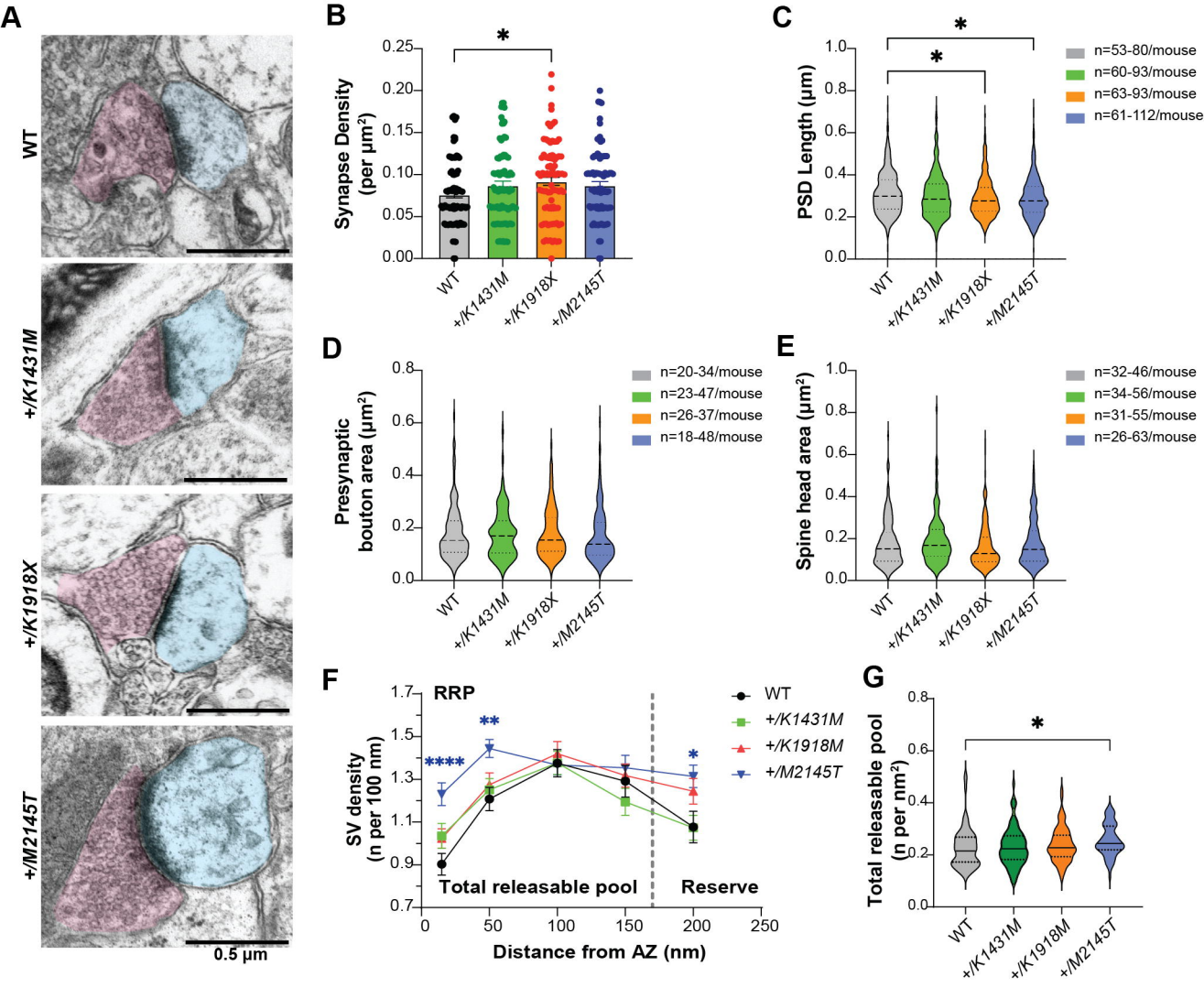
A
WT
+/K1431M
+/K1918X
+/M2145T
0.5 µm
B
Synapse Density (per µm²)
0.25
0.20
0.15
0.10
0.05
0.00
*
WT
+/K1431M
+/K1918X
+/M2145T
C
PSD Length (µm)
1.0
0.8
0.6
0.4
0.2
0.0
*
*
n=53-80/mouse
n=60-93/mouse
n=63-93/mouse
n=61-112/mouse
WT
+/K1431M
+/K1918X
+/M2145T
D
Presynaptic bouton area (µm²)
0.8
0.6
0.4
0.2
0.0
n=20-34/mouse
n=23-47/mouse
n=26-37/mouse
n=18-48/mouse
WT
+/K1431M
+/K1918X
+/M2145T
E
Spine head area (µm²)
1.0
0.8
0.6
0.4
0.2
0.0
n=32-46/mouse
n=34-56/mouse
n=31-55/mouse
n=26-63/mouse
WT
+/K1431M
+/K1918X
+/M2145T
F
RRP
SV density (n per 100 nm)
1.7
1.5
1.3
1.1
0.9
0.7
****
**
*
WT
+/K1431M
+/K1918M
+/M2145T
Total releasable pool
Reserve
0
50
100
150
200
250
Distance from AZ (nm)
G
Total releasable pool (n per nm²)
0.8
0.6
0.4
0.2
0.0
*
WT
+/K1431M
+/K1918M
+/M2145T

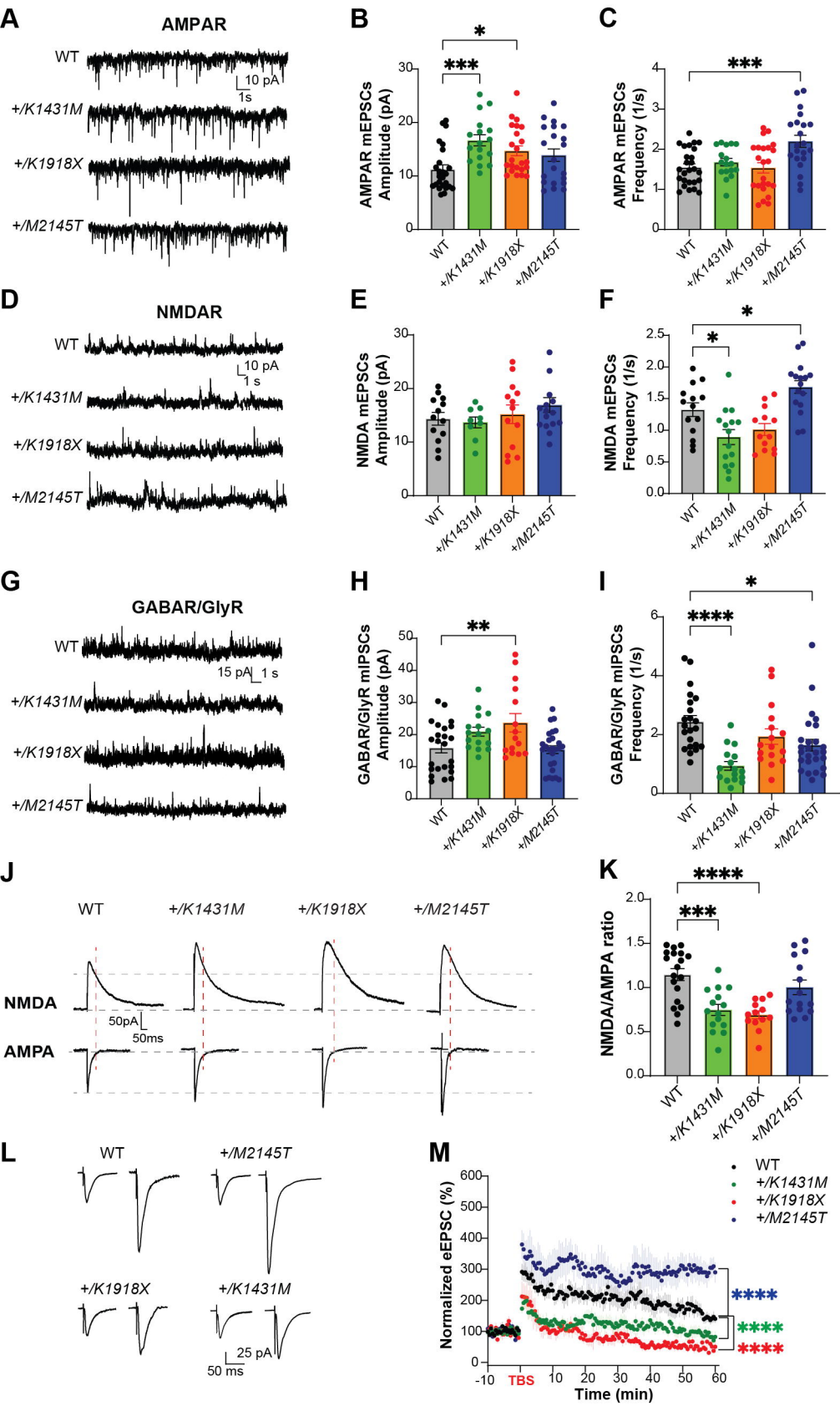
A
AMPAR
WT
+/K1431M
+/K1918X
+/M2145T
10 pA
1s
B
AMPAR mEPSCs Amplitude (pA)
C
AMPAR mEPSCs Frequency (1/s)
D
NMDAR
10 pA
1 s
E
NMDA mEPSCs Amplitude (pA)
F
NMDA mEPSCs Frequency (1/s)
G
GABAR/GlyR
15 pA
1 s
H
GABAR/GlyR mIPSCs Amplitude (pA)
I
GABAR/GlyR mIPSCs Frequency (1/s)
J
NMDA
AMPA
50pA
50ms
K
NMDA/AMPA ratio
L
25 pA
50 ms
M
Normalized eEPSC (%)
TBS
Time (min)

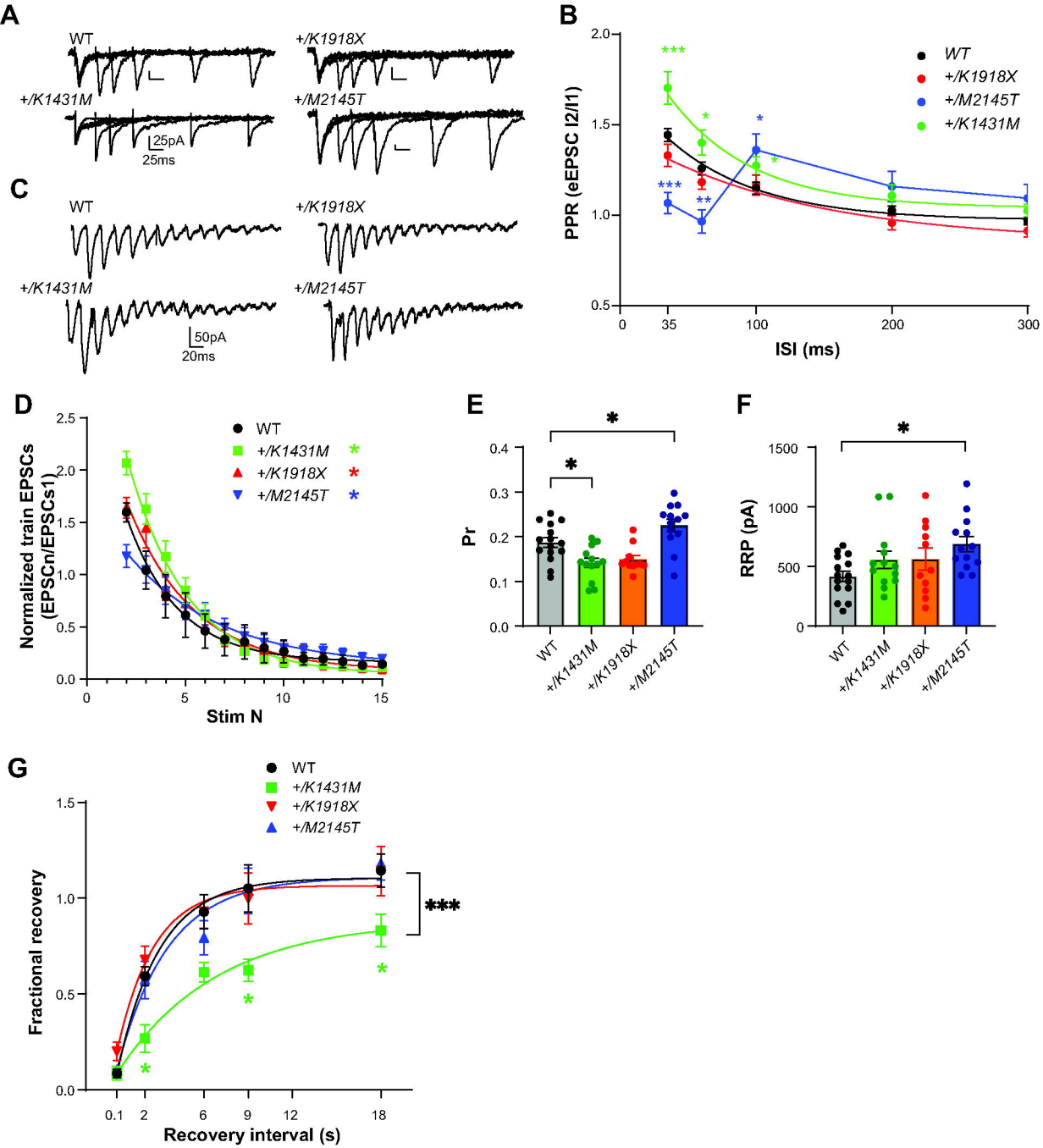

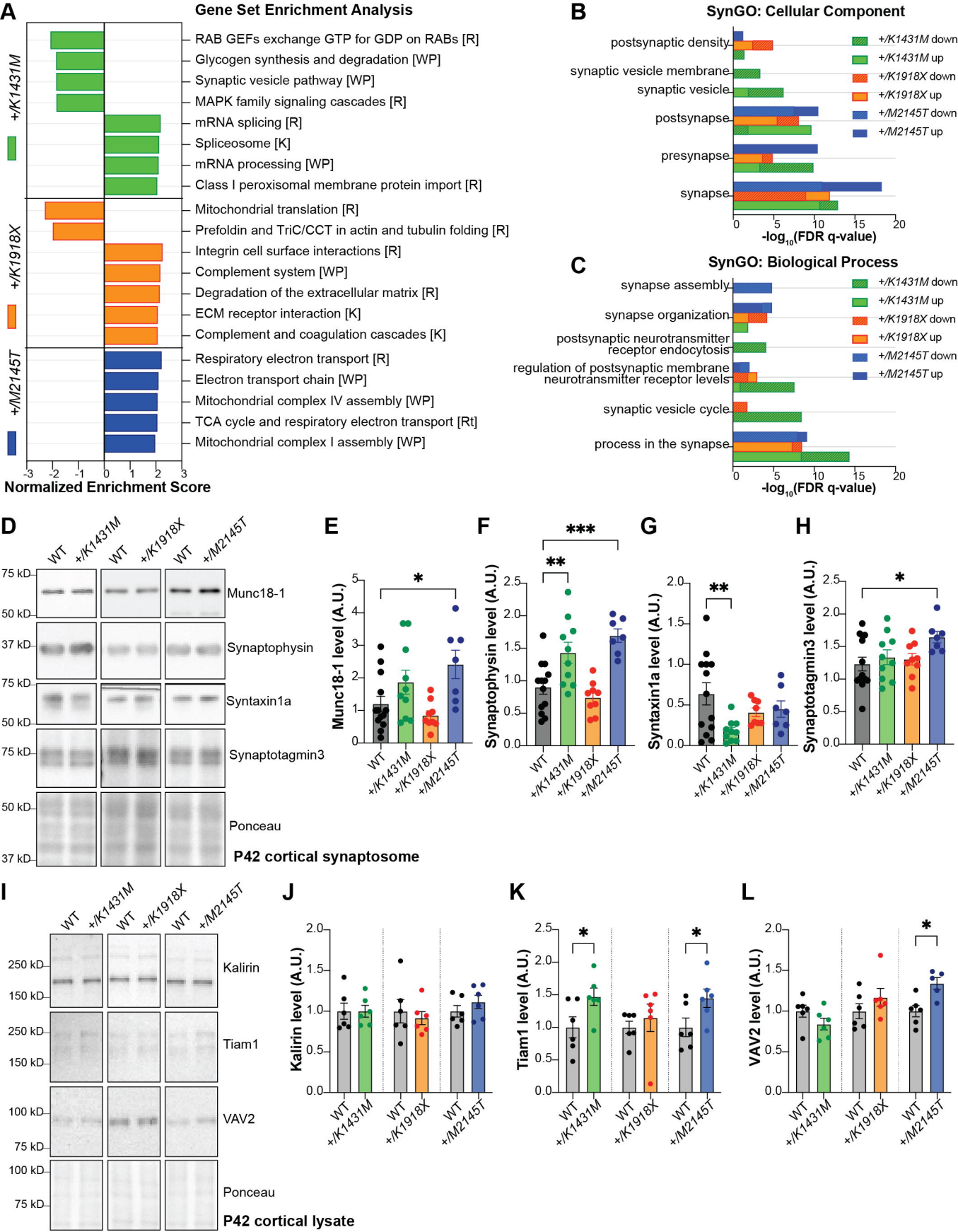
A
Gene Set Enrichment Analysis
+/K1431M
+/K1918X
+/M2145T
RAB GEFs exchange GTP for GDP on RABs [R]
Glycogen synthesis and degradation [WP]
Synaptic vesicle pathway [WP]
MAPK family signaling cascades [R]
mRNA splicing [R]
Spliceosome [K]
mRNA processing [WP]
Class I peroxisomal membrane protein import [R]
Mitochondrial translation [R]
Prefoldin and TriC/CCT in actin and tubulin folding [R]
Integrin cell surface interactions [R]
Complement system [WP]
Degradation of the extracellular matrix [R]
ECM receptor interaction [K]
Complement and coagulation cascades [K]
Respiratory electron transport [R]
Electron transport chain [WP]
Mitochondrial complex IV assembly [WP]
TCA cycle and respiratory electron transport [Rt]
Mitochondrial complex I assembly [WP]
-3 -2 -1 0 1 2 3
Normalized Enrichment Score
B
SynGO: Cellular Component
postsynaptic density
synaptic vesicle membrane
synaptic vesicle
postsynapse
presynapse
synapse
+/K1431M down
+/K1431M up
+/K1918X down
+/K1918X up
+/M2145T down
+/M2145T up
0 5 10 15 20
-log10(FDR q-value)
C
SynGO: Biological Process
synapse assembly
synapse organization
postsynaptic neurotransmitter receptor endocytosis
regulation of postsynaptic membrane neurotransmitter receptor levels
synaptic vesicle cycle
process in the synapse
+/K1431M down
+/K1431M up
+/K1918X down
+/K1918X up
+/M2145T down
+/M2145T up
0 5 10 15 20
-log10(FDR q-value)
D
WT
+/K1431M
WT
+/K1918X
WT
+/M2145T
75 kD
50 kD
37 kD
75 kD
50 kD
75 kD
50 kD
37 kD
Munc18-1
Synaptophysin
Syntaxin1a
Synaptotagmin3
Ponceau
P42 cortical synaptosome
E
Munc18-1 level (A.U.)
F
Synaptophysin level (A.U.)
G
Syntaxin1a level (A.U.)
H
Synaptotagmin3 level (A.U.)
WT
+/K1431M
+/K1918X
+/M2145T
I
WT
+/K1431M
WT
+/K1918X
WT
+/M2145T
250 kD
150 kD
250 kD
150 kD
100 kD
75 kD
100 kD
75 kD
Kalirin
Tiam1
VAV2
Ponceau
P42 cortical lysate
J
Kalirin level (A.U.)
K
Tiam1 level (A.U.)
L
VAV2 level (A.U.)
WT
+/K1431M
WT
+/K1918X
WT
+/M2145T